PAPER

Check for updates

Ni$_{0.5}$Co$_{0.5}$S nano-chains: a high-performing intercalating pseudocapacitive electrode in asymmetric supercapacitor (ASC) mode for the development of large-scale energy storage devices†

Vishal Kushwaha,[a] K. D. Mandal,[a] Asha Gupta (ID) *[a] and Preetam Singh (ID) *[b]

Grid-scale energy storage solutions are necessary for using renewable energy sources efficiently. A super-capapattery (supercapacitor + battery) has recently been introduced as a new variety of hybrid devices that engage both capacitive and faradaic charge storage processes. Nano-chain architectures of Ni$_{0.5}$Co$_{0.5}$S electrode materials consisting of interconnected nano-spheres are rationally constructed by tailoring the surface structure. Nano-chains of the bimetallic sulfide Ni$_{0.5}$Co$_{0.5}$S are presented to have a superior charge storage capacity. The Ni$_{0.5}$Co$_{0.5}$S nano-chain electrode presents a capacitance of 2001.6 F g^{-1} at 1 mV s^{-1}, with a specific capacity of 267 mA h g^{-1} (1920 F g^{-1}) at 1 A g^{-1} in 4 M KOH aqueous electrolyte through the galvanostatic charge–discharge (GCD) method. The reason behind the high charge storage capacity of the materials is the predominant redox-mediated diffusion-controlled pseudocapacitive mechanism coupled with surface capacitance (electrosorption), as the surface (outer) and intercalative (inner) charges stored by the Ni$_{0.5}$Co$_{0.5}$S electrodes are close to 46.0% and 54.0%, respectively. Additionally, a Ni$_{0.5}$Co$_{0.5}$S//AC two electrode full cell operating in asymmetric supercapacitor cell (ASCs) mode in 4 M KOH electrolyte exhibits an impressive energy density equivalent to 257 W h kg^{-1} and a power density of 0.73 kW kg^{-1} at a current rate of 1 A g^{-1}.

Introduction

Clean, pollution-free renewable energy technologies including solar, wind, and tidal have been developed in response to the gradual depletion of fossil fuels and the increase in CO$_2$ emissions but due to the time and weather dependent nature of these renewable energy technologies, a higher degree of current and voltage fluctuations is associated with these sources. Therefore, to get a steady electricity output from these sources, superior energy storage systems are needed to utilize such energy sources effectively. Thus, grid-scale energy storage devices are necessary to use renewable energy technology efficiently. Further large-scale energy

storage systems at high current rates are also required for electric vehicles, smart grids, and different wearable and portable gadgets.[1,2] Supercapacitors (SCs) have drawn a lot of attention due to their safer operation, rapid charge–discharge, and longer cycling life than traditional batteries and capacitors. The electrochemical characteristics of the electrode materials significantly impact the supercapacitor performance. Based on their energy storage mechanism, electrical double-layer capacitors (EDLCs) and pseudocapacitors (PCs) are the two main categories in their hybrid combinations to be used in SCs. Electrostatic charges accumulating at the electrode/electrolyte interface are the root of EDLC-type capacitance. Because the electrode materials used in pseudocapacitive energy storage with the accessibility of different oxidation states produce energy through swift and reversible redox processes, a substantially higher energy density than EDLCs is achieved.[3–6] Supercapapattery (supercapacitor + battery) which is another class of supercapacitors has recently been introduced as a new terminology to describe the variety of hybrid devices that engage both capacitive and faradaic charge storage processes either at the device level or the electrode material level. A supercapapattery is also known as an asymmetric supercapacitor (ASC) or hybrid supercapacitor (HSC) or battery-supercapacitor hybrid

[a]Department of Chemistry, Indian Institute of Technology (Banaras Hindu University) Varanasi, Uttar Pradesh, 221005, India. E-mail: asha.chy@itbhu.ac.in, toashagupta@gmail.com; Tel: +91-6390363140
[b]Department of Ceramic Engineering, Indian Institute of Technology (Banaras Hindu University) Varanasi, Uttar Pradesh, 221005, India.
E-mail: preetamsingh.cer@itbhu.ac.in, preetamchem@gmail.com;
Tel: +91-8118873748
†Electronic supplementary information (ESI) available. See DOI: https://doi.org/10.1039/d3dt04184k

device. In an HSC or ASC system, the power source of a capacitor-like electrode is combined with the energy source of a battery-like electrode in the same cell. The supercapattery bridges the gap between a supercapacitor and a battery by combining both capacitive and faradaic charge storage mechanisms into a single device that achieves optimal energy and power densities.[7,8] While supercapacitors have a high power capability and batteries have a massive capacity for energy storage, a supercapattery comprises a wide variety of combinations that are currently under exploration to develop large-scale energy storage systems.[9,10] To overcome low energy densities, low stability, and slow kinetics, strategic measures are required to be taken. In this context, significant research has been devoted to designing and fabricating several high-performance energy storage materials, such as Fe_2O_3,[11,12] MoS_2,[13–15] Co_3O_4,[16,17] $NaVO_3$,[18] V_2O_5,[19] Nb_2O_5,[20] MoO_3,[21–23] MnO_2[24] and transition-metal sulfides[25,26] in recent times. Due to their electronic structure and structural properties, TMSs have been extensively researched in optical, electrical and optoelectronic devices, including light-emitting diodes, solar cells, sensors and electrodes for lithium-ion batteries (LIBs).[27–31] Due to their low electronegativity, high specific capacitance, and superior mechanical and thermal stability compared to their analogous oxide counterparts, sulfides of transition metals, such as WS_2,[32–34] FeS_2,[35,36] MoS_2,[13–15] CuS,[37,38] CoS,[39–43] and NiS,[44–48] have been extensively employed as anode materials for supercapacitors. Because of its unique and distinctive properties, nickel sulfide is helpful in various applications and can serve as both the anode and cathode material for LIBs.[49,50] The use of cobalt sulfides as the cathode in LIBs has been examined as a robust material with a low overpotential, extended cycle life, high resilience, and durability.[51,52] Bimetallic sulfides are regarded as a promising class of electrode materials for high-performance energy storage devices due to their exceptional electrochemical activity and capacity compared to most mono-metal sulfides.[53–58] Due to their distinctive physical, chemical, electrical, and optical properties, as well as their numerous potential applications in catalysis and electrochemical supercapacitors, Ni–Co–S compounds with different stoichiometric compositions, such as $NiCo_2S_4$,[59–62] $CoNi_2S_4$,[63–65] $Ni_{1.5}Co_{1.5}S_4$,[66,67] $Ni_xCo_{3−x}S_4$,[68,69] $(Ni_{0.5}Co_{0.5})_9S_8$,[70] and $Ni_xCo_{1−x}S_2$,[71–73] have drawn significant attention.

Electrochemical activities can be maximized by altering the active material compositions, fine-tuning the electronic struc-

tures, and adjusting the active sites of materials. The ionic radius of Co^{2+} is close to that of Ni^{2+} as they are adjacent transition metal elements. Thus, doping Ni atoms onto the CoS molecule can regulate the electronic structure and stabilize Co species as the electrode material for supercapacitors. As the crystal structure and ionic radius are similar, a solid solution of $Ni_xCo_{1−x}S$ is expected to be formed. Earlier, C. Huang *et al.* attempted to construct bundle-like $Ni_xCo_{1−x}S/C$ nanostructures using 3D Ni–Co–BTC as the starting material to enhance the supercapacitive performance of the electrode.[73]

This report presents the synthesis and characterization of a bimetallic sulfide $Ni_{0.5}Co_{0.5}S$ nanostructure and the electrochemical performances of the developed $Ni_{0.5}Co_{0.5}S$ nano-chain electrodes. Due to the combined advantages of Co/Ni–S electronic structures, the $Ni_{0.5}Co_{0.5}S$ electrode demonstrated a significantly improved electrochemical performance. The electrode achieved a specific capacity of 267 mA h g^{-1} (1920 F g^{-1}) at 1 A g^{-1} in 4 M KOH aqueous electrolyte through galvanostatic charge–discharge (GCD) experiments and a capacitance equivalent to 2001.6 F g^{-1} at 1 mV s^{-1} by cyclic voltammetry (CV). Furthermore, the assembled $Ni_{0.5}Co_{0.5}S//AC$ asymmetric supercapacitors (ASCs), which employed the $Ni_{0.5}Co_{0.5}S$ electrode as the positive electrode and activated carbon (AC) as the negative electrode, obtained an impressive energy density comparable to ~257 W h kg^{-1} and a power density of ~7.2 kW kg^{-1}.

Experimental

Synthesis

All chemicals used in this experiment were purchased from Alfa Aesar and used without any further purification. To create a homogeneous solution, equimolar ratios of $NiCl_2·6H_2O$ and $CoCl_2·6H_2O$ were dissolved in 250 ml of deionized water and continuously stirred for 5–6 hours, followed by ultrasonication for 30 minutes. Then, a black fine precipitate was obtained when H_2S gas was introduced into the solution using the Kipp generator technique. A schematic illustration of the synthesis of $Ni_{0.5}Co_{0.5}S$ is shown in Fig. 1.

The resultant fine precipitate was filtered and repeatedly washed with ethanol and deionized water. The product was then dried in a hot air oven (under an N_2 atmosphere) at
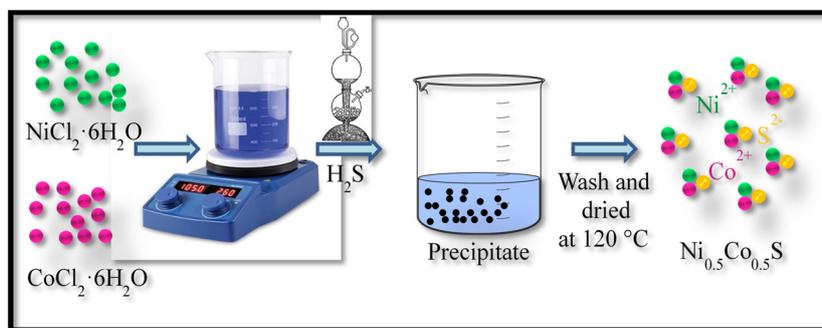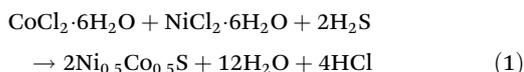

Fig. 1 Schematic presentation of the synthesis of $Ni_{0.5}Co_{0.5}S$.

120 °C for 24 hours and used for crystallographic and electrochemical characterization. The chemical reaction representing the formation of $Ni_{0.5}Co_{0.5}S$ is given in eqn (1).

$$CoCl_2 \cdot 6H_2O + NiCl_2 \cdot 6H_2O + 2H_2S$$
$$\rightarrow 2Ni_{0.5}Co_{0.5}S + 12H_2O + 4HCl \qquad (1)$$

Characterization

Using a Rigaku SmartLab 9 kW X-ray diffractometer (XRD) and Cu-Kα radiation (λ = 0.154 nm) in the range 2θ = 20°–70° with a step size of 0.02°, the material's phase purity and structural characteristics were investigated. Using FullProf Suite, the powder XRD patterns were Rietveld refined. The Xpert High Score (PANanylytical) programme identified the crucial phase. The surface morphology and structure of the sample were studied using SEM (EVO-Scanning Electron Microscope MA15/18, CARL ZEISS Microscopy Ltd). Microstructural analyses were carried out at a 200 kV acceleration voltage using a high-resolution transmission electron microscope (FEI Tecnai G^2 20 TWIN, USA). Before placing a drop on a holey-carbon-coated copper grid (Pelco International, USA) for TEM imaging, samples were dissolved in 20 ml of anhydrous ethanol and sonicated for 30 minutes. Image J software was used to record and analyse HRTEM micrographs. Using an Agilent Cary 60 UV-visible spectrophotometer, the optical characteristics between 200–800 nm were investigated. Using a TGA thermal analyzer (STA 6000, PerkinElmer Pvt. Ltd), the analysis was conducted at a heating rate of 10 °C min^{-1} in the temperature range of 30 to 700 °C to determine the thermal stability of the as-prepared sample. The sample's Raman spectra were calculated using a 633 nm laser and a Renishaw Raman microscope. The Nicolet iS5 FT-IR spectrometer was used to capture the samples' infrared spectra between 400 and 4000 cm^{-1}. BET (BELCAT-II, MicrotracBEL Corp.) was used to measure the sample's pore size distribution and specific surface area. A standard three-electrode setup was used to conduct all electrochemical tests on the sample, including cyclic voltammetry (CV), galvanostatic charge–discharge (GCD) tests, and electrochemical impedance spectroscopy (EIS), and AfterMath software (WaveDriver-200 from Pine Research) was used to record the results.

Preparation of the electrode

The appropriate amounts of the active material, activated carbon (AC), and polyvinylidene difluoride (PVDF) binder were combined in N-methyl-2-pyrrolidone (NMP) solvent in the ratio of 7 : 2 : 1 to prepare working electrodes. Active material ($Ni_{0.5}Co_{0.5}S$) was preheated at 120 °C for 24 h in a hot air oven before making the electrode ink. To construct the working electrode, a homogeneous, viscous slurry was mixed using a mortar and pestle and then cast over a 1 cm^2 area of Toray carbon paper. Additionally, the coated electrode was dried for 12 hours at 80 °C. In the fabrication of the electrodes, AC was employed to improve the conductivity of the electrodes. The electrode loading was estimated by weighing the electrode on an electronic balance (error limit: 0.01 mg). For that, the weight of the Toray paper was recorded, and then the Toray paper was coated with electrode ink (after the ink had dried across a 1 × 1 cm^2 area on the Toray paper). One mg was found to represent the complete electrode load (0.7 mg active material, 0.2 mg AC, and 0.1 mg PVDF binder). Similarly, the required amounts of AC and PVDF binder were dissolved in NMP solvent in a 9 : 1 ratio to produce AC electrodes.

Results and discussion

Structural characterization

The single-phase hexagonal $Ni_{0.5}Co_{0.5}S$ sample was synthesized using a simple H_2S-mediated two-phase (gas diffusion in liquid) precipitation route in an aqueous medium. The formation of $Ni_{0.5}Co_{0.5}S$ in a single phase is facilitated by the controlled heterogeneous precipitation of the solid phase due to the gradual diffusion of H_2S gas into the liquid phase. Fig. 2a shows the Rietveld refined XRD profile of the hexagonal $Ni_{0.5}Co_{0.5}S$. The crystal structure was refined using hexagonal CoS as the model structure. The sharp prominent diffraction peaks at 2θ values of 30.67, 35.34, 46.95, 54.52, 62.56, 63.87, 66.65, 73.12 and 74.75 represent the (100), (101), (102), (110), (103), (200), (201), (004), and (202) planes, respectively, of $Ni_{0.5}Co_{0.5}S$ in the hexagonal cell (space group: $P6_3/mmc$) with lattice parameters $a = b$ = 3.37 (1) Å, c = 5.18 (3) Å, $\alpha = \beta$ = 90° and γ = 120°, which match very well with the diffraction peaks of hexagonal CoS (ICDD File No: 01-075-0605). The VESTA images (Fig. 2b-I$_1$, I$_2$ and I$_3$) of the $Ni_{0.5}Co_{0.5}S$ nano-chains show the arrangement and sharing of cation polyhedra in a layered hexagonal structure. The Co^{2+}/Ni^{2+} atom is bonded to six equivalents of S^{2-} atoms to form a mixture of corner, edge and face sharing octahedra. Furthermore, the S^{2-} atom is bonded in a 6 coordinate geometry to 6 equivalents of Co^{2+}/Ni^{2+} atoms. The Debye–Scherrer equation was used to evaluate the crystallite size, and an average crystallite size of 21.07 (1) nm was found. Due to the substitution of smaller Co^{2+} ions ($r_{Co^{2+}}$ = 0.065 nm) with the larger Ni^{2+} ions ($r_{Ni^{2+}}$ = 0.069 nm) in the hexagonal CoS structure, lattice parameters of $Ni_{0.5}Co_{0.5}S$ are shifted to a higher value than those of hexagonal CoS.[73] The XRD pattern of the $Ni_{0.5}Co_{0.5}S$ sample confirms the presence of single-phase hexagonal (space group: $P6_3/mmc$) $Ni_{0.5}Co_{0.5}S$ as no secondary diffraction phases are observed.

Thermogravimetric analysis (TGA) under an N_2 atmosphere investigated the sample's thermal stability, as shown in ESI Fig. S1a.† The $Ni_{0.5}Co_{0.5}S$ sample's black powder was subjected to heating from ambient temperature to 700 °C with a heating rate of 10 °C per minute. The weight loss process of the $Ni_{0.5}Co_{0.5}S$ nano-chains may be separated into two distinct phases. The first phase of weight loss occurs within the temperature range of 65–135 °C, resulting in a weight loss of about 6.06%, equivalent to ~0.45 H_2O molecules. The observed reduction in weight may be ascribed to the presence of physically adsorbed moisture and the hydroxide group. From 135 °C to 533 °C, the sample is almost stable, with a slight
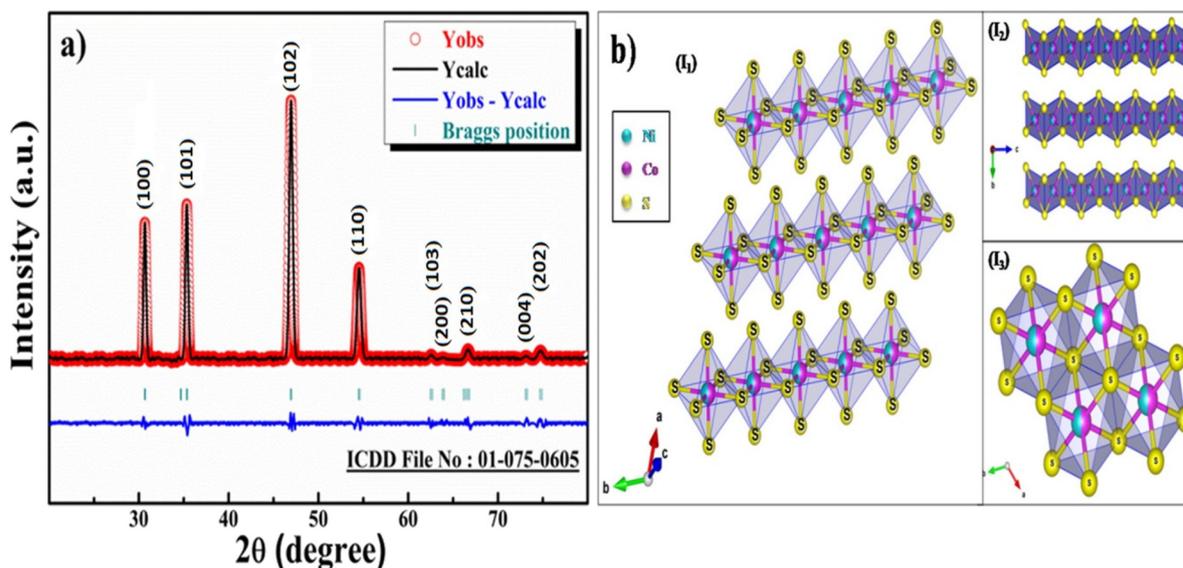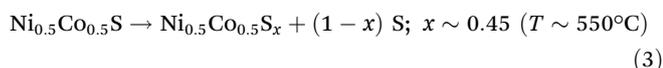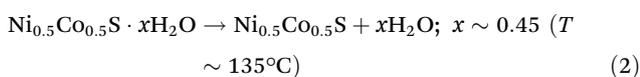
Fig. 2 (a) Rietveld refinement of the XRD profile of $Ni_{0.5}Co_{0.5}S$ nano-chains, and (b) VESTA image of $Ni_{0.5}Co_{0.5}S$ nano-chains.

weight loss, which implies that the $Ni_{0.5}Co_{0.5}S$ nano-chains are stable up to a fairly high temperature. Additionally, at a temperature of 533 °C, a significant reduction in weight occurs due to the disintegration of the $Ni_{0.5}Co_{0.5}S$ nano-chains, resulting in the release of sulfur. A weight loss of 17.81% accompanies this decomposition process.[74,75] Hence to remove the water present in the sample, the sample was dried at 120 °C under an N_2 atmosphere to make it moisture free to study the electrochemical performances of the electrode. Eqn (2) and (3) in the TGA study depict the observed weight losses.

$$Ni_{0.5}Co_{0.5}S \cdot xH_2O \rightarrow Ni_{0.5}Co_{0.5}S + xH_2O; \ x \sim 0.45 \ (T \sim 135°C) \quad (2)$$

$$Ni_{0.5}Co_{0.5}S \rightarrow Ni_{0.5}Co_{0.5}S_x + (1 - x) \ S; \ x \sim 0.45 \ (T \sim 550°C) \quad (3)$$

The FT-IR spectrum of the as-prepared (without any pre-heating) $Ni_{0.5}Co_{0.5}S$ nano-chains is shown in ESI Fig. S1b.† The spectral peaks at 3347 cm^{-1} and 1631 cm^{-1} may be attributed to the stretching and bending vibrations of the hydroxyl (OH) functional group of water molecules that have been adsorbed onto the surface. Furthermore, the bands at 407, 414, 421, and 433 cm^{-1} are related to the symmetrical stretching vibration, whereas those at 1016 and 1085 cm^{-1} are related to the asymmetrical stretching vibration assigned to Ni–S or Co–S bonds in the $Ni_{0.5}Co_{0.5}S$ sample.[4,76]

For additional investigation on the structure and phase composition of the sample, Raman spectroscopy was performed on the pre-heated active material as shown in ESI Fig. S1c.† Peaks at 180, 455, 513, and 640 cm^{-1} can be indexed to the Raman-active vibrational peaks of the $Ni_{0.5}Co_{0.5}S$ sample, which correspond to the typical phonon modes F_{2g}, E_g, T_{2g} and A_{1g}, respectively.[77,78] The Raman spectral lines of

the $Ni_{0.5}Co_{0.5}S$ sample exhibited a shift towards lower wave numbers, often referred to as a bathochromic shift or red shift. This shift indicates the phonon confinement effect, which may be attributed to the quantum confinement of optical phonons. This effect is further corroborated by a high-intensity stretching band seen at a wavenumber of 962 cm^{-1}.[4]

The UV-visible absorption spectrum of the as-synthesized pre-heated $Ni_{0.5}Co_{0.5}S$ was recorded at room temperature in the range of 200–800 nm (ESI Fig. S1d†). The absorption peak at a wavelength of 374 nm was seen, and the optical band gap (2.32 eV) was determined using the Tauc plot (shown in the inset of ESI Fig. S1d†).[79] The surface area measurements of the $Ni_{0.5}Co_{0.5}S$ sample using Brunauer–Emmett–Teller (BET) are displayed in ESI Fig. S1e.† The adsorption and desorption isotherms of the $Ni_{0.5}Co_{0.5}S$ sample showed characteristics that correspond to type IV isotherms, indicating a combination of micro- and mesoporous structures. The calculated BET-specific surface area and the average diameters of pores were found to be 13.45 $m^2 \ g^{-1}$ and 14.27 nm, respectively. The $Ni_{0.5}Co_{0.5}S$ sample exhibits mesopores characterized by a significantly enhanced surface area. This attribute facilitates an enhanced interaction with the electrolyte and improves electrochemical reaction kinetics. The increased concentration of charge carriers at the material's surface is responsible for this effect. Furthermore, it is shown that the measured mesopore diameter of the $Ni_{0.5}Co_{0.5}S$ nano-chains is much larger than the dimensions of OH-ions in an aqueous KOH electrolyte.[73,80]

The elemental composition and chemical oxidation state of the $Ni_{0.5}Co_{0.5}S$ nano-chains were studied using X-ray photoelectron spectroscopy (XPS). The spectrum shown in Fig. 3a exhibits the high-resolution Ni (2p) spectrum. It reveals the presence of two distinct peaks, namely $2p_{3/2}$ and $2p_{1/2}$, located at 856.74 and 874.34 eV, with their corresponding satellite peaks at 862.46 and 880.23 eV, respectively, assigned to the
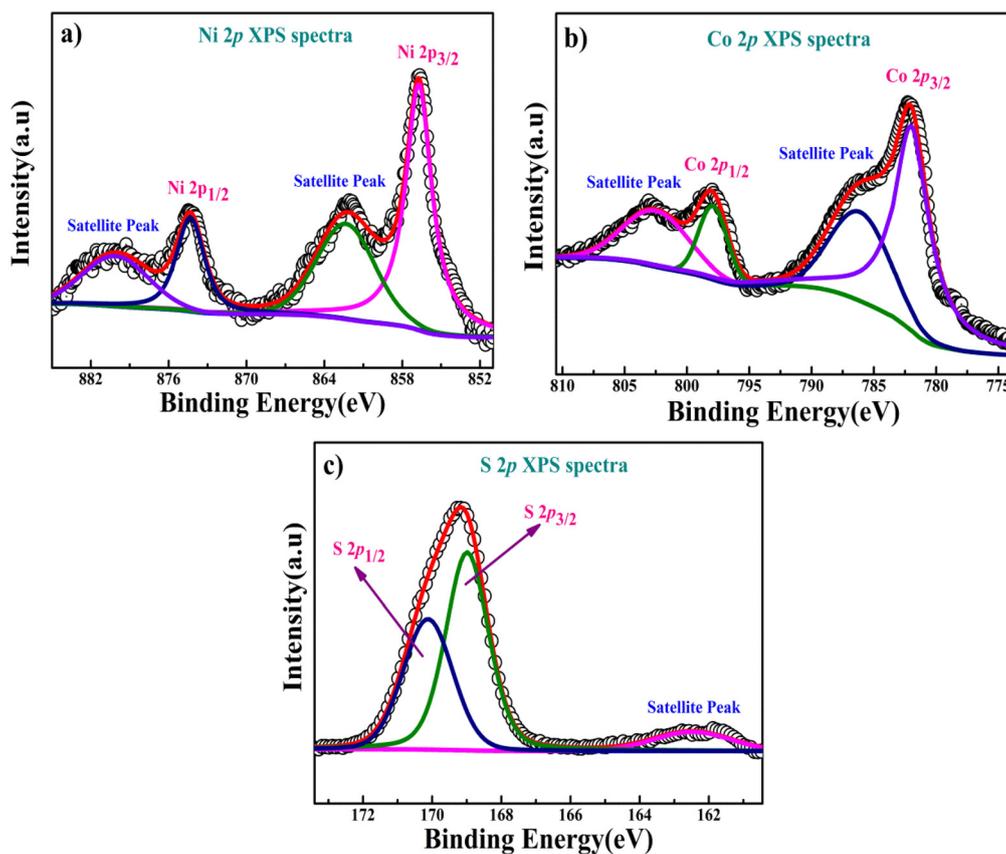
Fig. 3 XPS plot of $Ni_{0.5}Co_{0.5}S$ nano-chains, (a) Ni (2p) spectra, (b) Co (2p) spectra, and (c) S (2p) spectra.

Ni^{2+} oxidation state. Likewise, the high-resolution Co (2p) spectrum (Fig. 3b) shows $2p_{3/2}$ and $2p_{1/2}$ at 782.05 and 797.96 eV, and the corresponding satellite peaks at 786.47 and 802.89 eV are assigned to the Co^{2+} oxidation state. The high-resolution S (2p) spectrum (Fig. 3c) shows two characteristic peaks at 168.98 and 170.12 eV, respectively. The peak observed at 168.98 eV corresponds to S $(2p_{3/2})$ associated with the sulfur–metal bonding and the peak that appeared at 170.12 eV corresponds to S $(2p_{1/2})$ and is attributed to the surface bonding of low-coordination divalent sulfur (S^{2-}). Furthermore, the satellite peak observed at about 162.52 eV corresponds to the binding energies of metal–sulfur bonding (Ni–S and Co–S bonding). Thus, the XPS study confirms the formation of Co^{2+}, Ni^{2+}, and S^{2-} oxidation states in the $Ni_{0.5}Co_{0.5}S$ sample.[64,67]

Fig. 4a shows the SEM image, which illustrates the particle dispersion and agglomerated arrangements of the $Ni_{0.5}Co_{0.5}S$ sample containing interconnecting spheres of sub-micron sizes. The EDX (energy dispersive X-ray) image shown in Fig. 4b confirms the composition of the material. HR-TEM images shown in Fig. 4(c and d) confirm the formation of the nano-chain arrangement of the $Ni_{0.5}Co_{0.5}S$ sample containing the interconnecting nanospheres. HR-TEM images of several other areas of the $Ni_{0.5}Co_{0.5}S$ sample are provided in the ESI Fig. S2 (a, b and c)† further confirming the successful formation of nano-chains. In aqueous solution, reduction in

coordination number of Ni^{2+}/Co^{2+} cations located on the corner occurs during the sulphide formation reaction at surfaces. Hence, the edge sites of sulphide (Ni/CoS) nuclei act as the active sites to react with S^{2-} anion relese through slow diffusion H_2S in aqueous solution preferentially form chain-like sulfide nuclei resulting in formation of $Ni_{0.5}C_{0.5}S$ nano-chains. The nano-chains' average diameter was ~60 nm as seen in the HRTEM images. The nano-chain structure can allow a fast electron transfer within the material required for a high rate/fast electrochemical capacitance/charge storage of the materials. The development of nano-chain architectures in $Ni_{0.5}Co_{0.5}S$ electrode materials is significant because it has the potential to enhance the electrode's performance by reducing the diffusion length, facilitating a larger surface area for contact between the active materials and the electrolyte, and improving the kinetics of electrochemical reactions, leading to improved energy storage and conversion properties.[81]

Electrochemical studies

The electrochemical behavior was investigated using galvanostatic charge–discharge and cyclic voltammetry (CV) to evaluate the capability and suitability of the material for energy storage as supercapacitors. The charge-storage properties of the $Ni_{0.5}Co_{0.5}S$ electrodes were evaluated using cyclic voltammetry (CV) in a three-electrode setup. The counter electrode

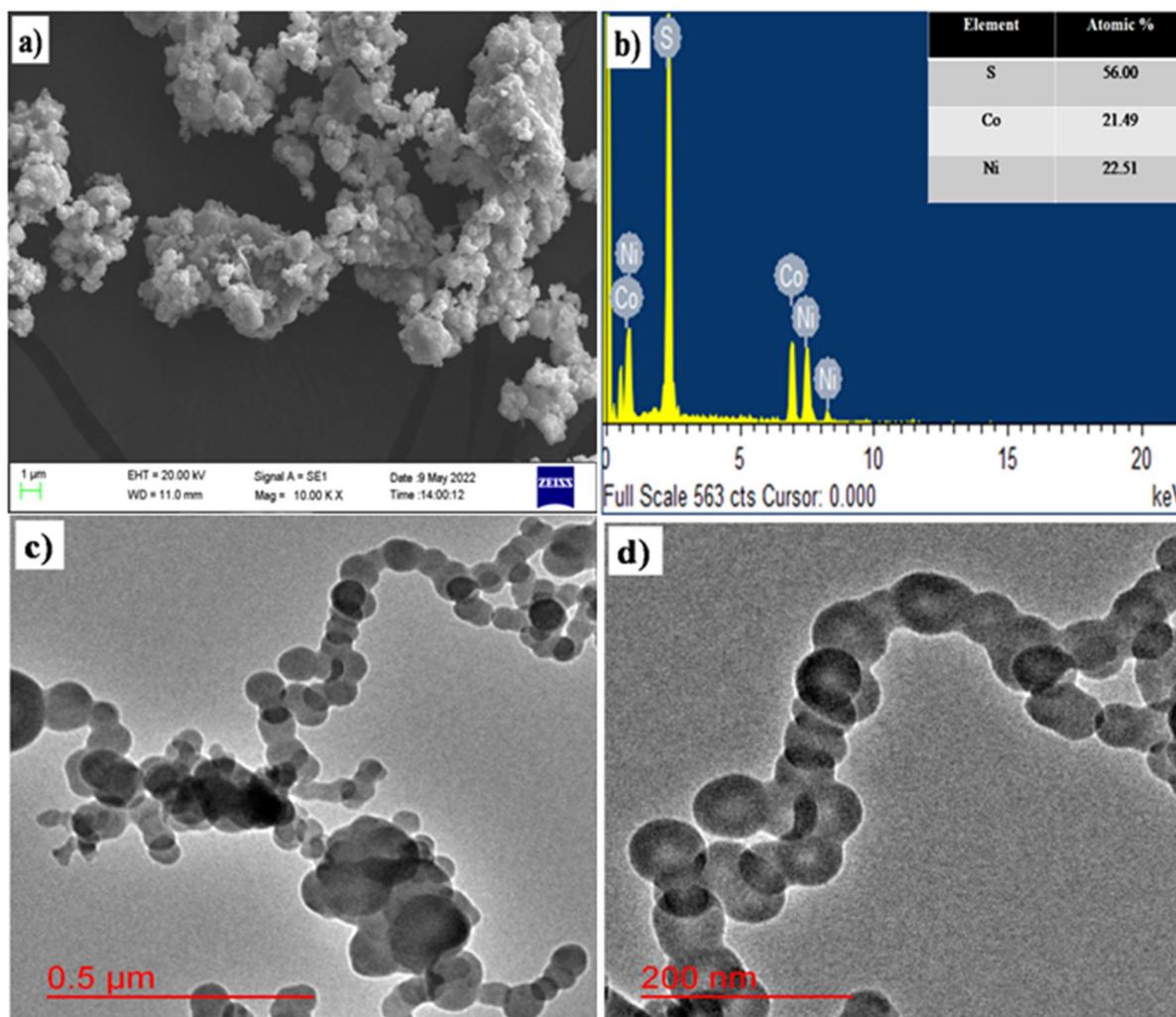| Element	Atomic %
S	56.00
Co	21.49
Ni	22.51

Fig. 4 (a) SEM images, (b) EDX analysis image of the prepared $Ni_{0.5}Co_{0.5}S$ nano-chains, (c and d) HRTEM images of $Ni_{0.5}Co_{0.5}S$ nano-chains.

consisted of a platinum electrode; the working electrode was a $Ni_{0.5}Co_{0.5}S$ nano-chain coated carbon paper with an area of $1\ cm^2$. In contrast, a saturated Hg/HgO electrode in 1 M KOH solution was used as the reference electrode in the KOH electrolyte. The electrochemical parameters of the working electrode can be analyzed by calculating the charge storage capacity of the materials using eqn (4) in conjunction with the CV curve.

$$C_{sp} = \frac{\int_{E_1}^{E_2} i\ (E)\mathrm{d}E}{2mv(E_2 - E_1)} \qquad (4)$$

The calculation of the charge storage capacity in mA h g^{-1} can be determined using eqn (5).

$$C(\mathrm{mAh\ g^{-1}}) = C_{sp}\Delta V/3.6 = \frac{\int_{E_1}^{E_2} i\ (E)\mathrm{d}E}{2mv \times 3.6} \qquad (5)$$

In this equation, C_{sp} is the specific charge storage capacitance in F g^{-1}, the integral $\int_{E_1}^{E_2} i(E)\mathrm{d}E$ is the total voltammetric

charge acquired by integrating both positive and negative sweeps in CV, $(E_2 - E_1)$ is the width of the potential window (V), m is the mass (g) of the active material, and v is the scan rate (V s^{-1}). Although the capacitance values in the forward and backward directions do not precisely match, we have used the average value; as a result, the factor 1/2 is employed to create the holistic picture. The CV data were collected at different KOH concentrations, namely 0.5, 1, 2, 4, and 6 M. Fig. 5(a–d) illustrates the CV plot between the concentration of KOH and the mass-specific capacitance. The mass-specific capacitances were determined using eqn (4) and (5) and were found to be 1512, 1580, 1836, 2001.6, and 1703 F g^{-1} at a scan rate of 1 mV s^{-1} in KOH solutions with different concentrations ranging from 0.5, 1, 2, 4, to 6 M, respectively.

As seen in Fig. 5a, the specific capacitance exhibits an initial upward trend as the OH^- concentration increases and reaches its peak capacitance in a 4 M KOH solution. Subsequently, the particular capacitance diminishes with further escalation of the OH^- concentration. The $Ni_{0.5}Co_{0.5}S$

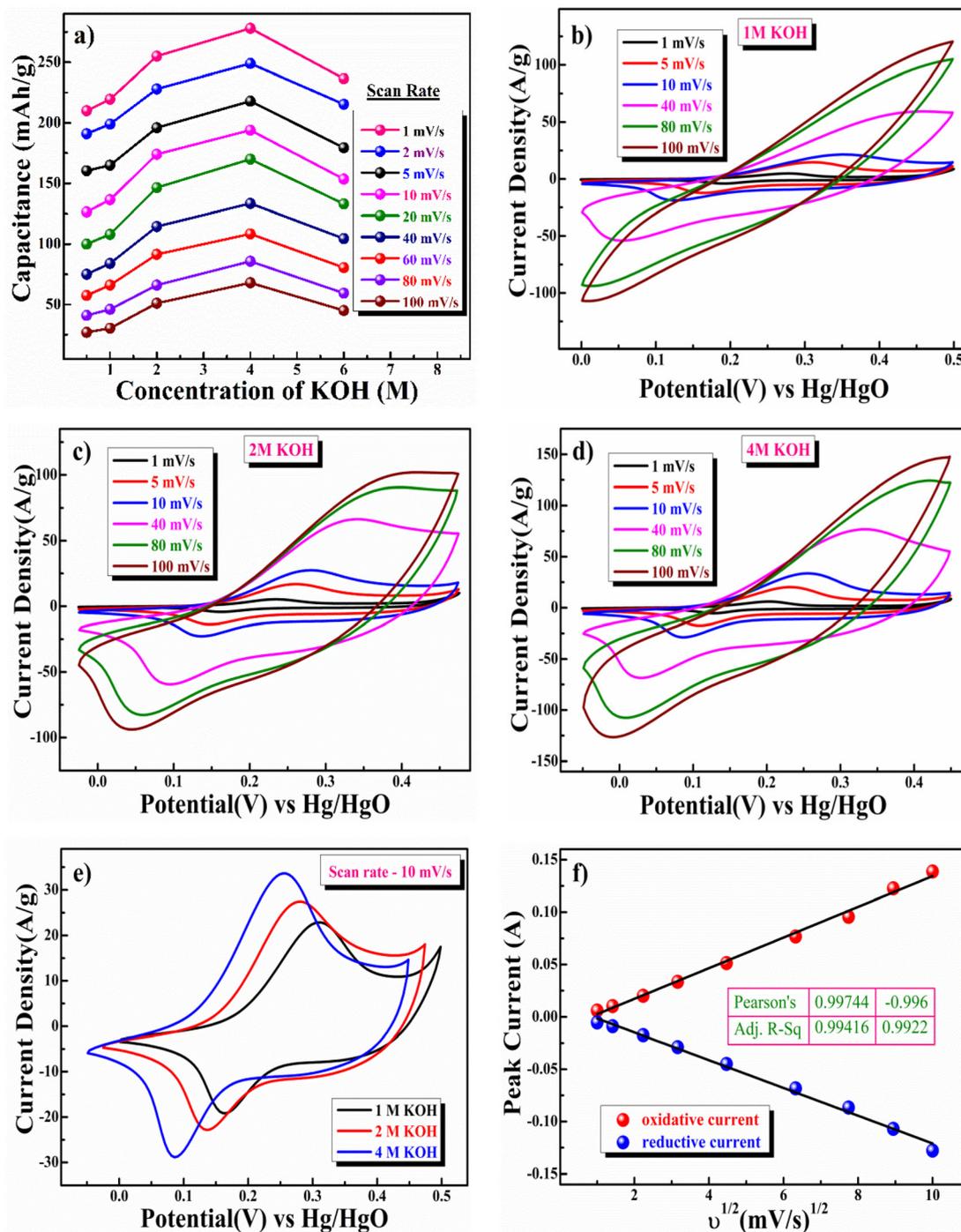**Fig. 5** (a) The plot of KOH concentrations *vs.* specific capacitance at various sweep rates. Standard CV plots for the Ni$_{0.5}$Co$_{0.5}$S electrode in (b), (c), and (d) solutions of 1, 2, and 4 M KOH at different sweep rates of 1–100 mV s^{-1}. The comparative CV analysis at 10 mV s^{-1} (e), and the Ni$_{0.5}$Co$_{0.5}$S electrode diffusion kinetics plot (f).

sample has a higher specific capacitance in 4 M KOH due to the optimum number of charged ions trapped/stored on the porous surface. The electrolyte's ionic conductivity decreases when its concentration exceeds 4 M KOH. This decrease can be attributed to the slow migration of ions primarily due to the high probability of ion collision and the strong electrostatic interaction between anions and cations, leading to the sluggish formation of a double layer or surface absorptions of ions, resulting in a lower specific capacitance of the material in 6 M KOH electrolyte.[82–85]

One pair of clearly distinct redox peaks, located at +0.20/+0.12 V, is visible on the CV curve in Fig. 5d (4 M KOH).

The pseudocapacitive behavior in conjunction with surface redox (electrosorption) is explained by the CV curve's nature.[86] Thus non-rectangular and quasi-reversible curves were obtained in the potential range of −0.05 to +0.45 V, demonstrating that surface redox intercalation followed pseudocapacitive storage. Redox peaks are the result of the electrochemical charge transfer reaction involving the interconversion of Co^{2+} to Co^{3+} and Ni^{2+} to Ni^{3+} reversibly through electrosorption (redox) of OH^- ions. Furthermore, the redox activity increases with the substitution of Ni atoms at the Co-site of the CoS base structure. The synergistic interaction between Co and Ni leads to a very high charge storage capacity of the $Ni_{0.5}Co_{0.5}S$ electrode. The following chemical reaction equation is responsible for the redox-mediated charge storage on the electrode.[73]

$$Ni_{0.5}^{2+}Co_{0.5}^{2+}S + OH^- = Co_{0.5}^{3+}Ni_{0.5}^{3+}S(OH^-) + e^- \quad (6)$$
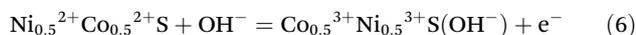
Later studies were carried out in 4 M KOH electrolyte only as the best activity of the electrode was found in this electrolyte. The capacitance of a 4 M KOH solution was determined by measuring it at various scan rates ranging from 1, 5, 10, 20, 40, 80, and 100 mV s^{-1} and the corresponding capacitance values were found to be 2001.6, 1569.6, 1397, 1224, 960.5, 617, and 489.6 F g^{-1}, respectively.

The specific capacitance decreases as the scan rates increase due to incomplete absorption coupled with surface redox at high scan rates. As the scan rate increases, the cathodic and anodic peaks shift linearly to a negative and positive potential, respectively. At the same time, the almost unchanged shapes of each curve demonstrated the high reversibility and rapid charge–discharge response of the $Ni_{0.5}Co_{0.5}S$ electrode. The capacitance retention for a 4 M KOH solution decreases to 31.25% as the scan rate increases from 1 to 100 mV s^{-1}. This decline may be attributed to the insufficient period available for the absorption and diffusion of ions into the active electrode surfaces at higher scan rates. Fig. 5e displays the comparative study of CV at different electrolyte concentrations, spanning from 1 M to 4 M. The redox potential is shifted to a lower value as the concentration of electrolyte (KOH) increases. This phenomenon is considered unfavourable in the context of high-voltage supercapacitor applications.[73,82]
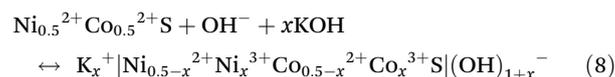
The relationship between cathodic and anodic peak currents in Fig. 5f indicates a linear correlation with the square root of scan rate ($v^{1/2}$). This observation suggests that the CV curve exhibits a behaviour governed by semi-infinite diffusion. The computation of the diffusion coefficient may achieve a more comprehensive understanding of electrode diffusion. The diffusion coefficient of the electrode was obtained using the Randles–Sevick equation (eqn (7)).

$$i_p = 2.686 \times 10^5 \times n^{3/2}AD^{1/2}C_0 v^{1/2} \quad (7)$$

In this equation, i_p is the peak current (A), n is the number of electrons transferred during the redox reaction (usually ~1), A is the area of the electrode in cm^2, D is the diffusion coefficient in cm^2 s^{-1}, C_0 is the concentration of OH^- ions in mol cm^{-3}, and v is the scan rate in V s^{-1}. The hydroxide (OH^-) ion diffusion coefficient (D) was found to be 3.14×10^{-8} cm^2 s^{-1} for oxidation and 2.50×10^{-8} cm^2 s^{-1} for reduction, respectively.

With $1e^-/OH^-$ charge transfer associated with reversible intercalation/de-intercalation of OH^- ions, the $Ni_{0.5}Co_{0.5}S$ electrode has a theoretical capacity of 1062 F g^{-1}, in the voltage window of −0.05 to 0.45 V. In our investigation, $Ni_{0.5}Co_{0.5}S$ demonstrated a consistent capacitance of 278 F g^{-1} at the scan rate of 1 mV s^{-1}. The $Ni_{0.5}Co_{0.5}S$ electrode exhibited a capacitance of 960.5 F g^{-1} even at a scan rate of 40 mV s^{-1}. Thus, the capacitance of $Ni_{0.5}Co_{0.5}S$ can be described as a combination of double-layer formation coupled with diffusion-controlled surface redox reactions. The electrochemical charge storage reaction is depicted in eqn (8) representing the contribution of both (1) double-layer formation and (2) diffusion-controlled surface redox processes.

$$Ni_{0.5}^{2+}Co_{0.5}^{2+}S + OH^- + xKOH$$
$$\leftrightarrow K_x^+|Ni_{0.5-x}^{2+}Ni_x^{3+}Co_{0.5-x}^{2+}Co_x^{3+}S|(OH)_{1+x}^- \quad (8)$$

The value of x can vary with the scan rates. The contribution of both (1) double-layer formation and (2) diffusion-controlled surface redox processes are determined in later studies. As we know, the charge storage of the electrode is mainly composed of two parts: the surface-controlled double-layer formation and the diffusion-controlled redox process. The charge storage mechanisms/kinetics of the $Ni_{0.5}Co_{0.5}S$ electrode was further evaluated qualitatively using the power law outlined in eqn (9).[73,87]

$$i = av^b \quad (9)$$

where a & b are variables that can be adjusted, i represents the current (A) and v is the scan rate (V s^{-1}). The value of b falls within the range of 0.5–1. A value of b equal to 1 represents the capacitive reaction or electrosorption at the surface. In contrast, a value of b equal to 0.5 means the reaction is controlled by semi-infinite diffusion, specifically for battery materials of the intercalative type. The b values for the oxidative and reductive currents, obtained from Fig. 6a, were determined to be 0.67 and 0.68, respectively, in the log(v) vs. log(i) plot. This indicates that the current can be attributed to a combination of diffusion-controlled insertion and pseudocapacitive processes (diffusion-controlled redox-mediated intercalation processes). Trasatti's[88] and Dunn's[89] methodologies evaluate the impacts of diffusion-controlled and surface-controlled capacitance processes on the obtained experimental data. Fig. 6b illustrates the dependency of the current response on the sweep rate in quantitative voltammetry, which enables the determination of the capacitive contribution. Diffusion-controlled insertion/intercalation and surface capacitive reactions contribute differently to the current response at a fixed potential.[90]

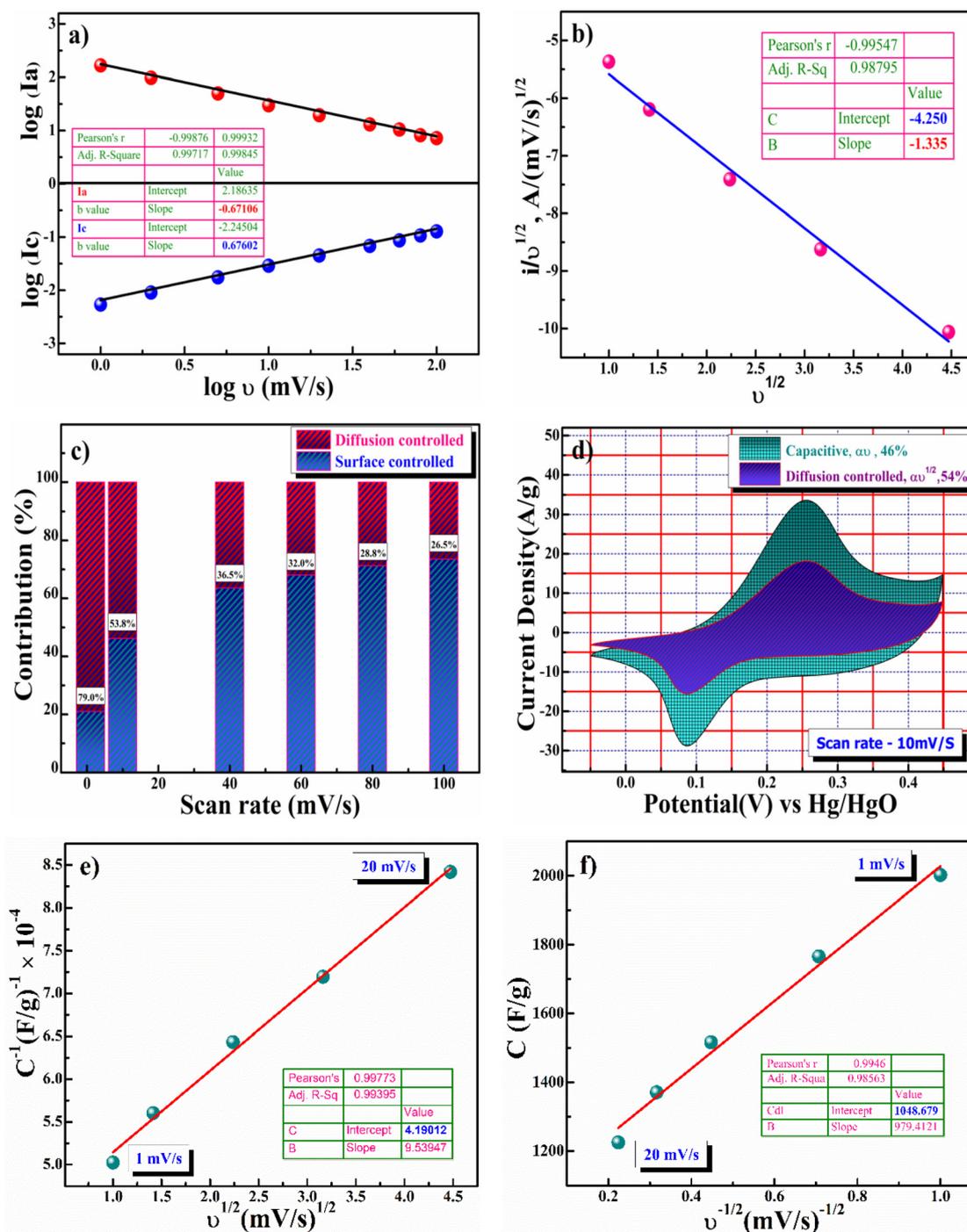$$i(v) = k_1 v + k_2 v^{1/2} \quad (10)$$

Fig. 6 Electrochemical dynamics of the $Ni_{0.5}Co_{0.5}S$ electrode; (a) the graph of log (peak current) vs. log (scan rate) at two different sweep rate parts, (b) the power law graph, (c) the capacitive and diffusive contribution at various sweep rates, (d) assessment of specific capacitance contribution at 10 mV s^{-1}, and (e and f) the Trasatti graph at various sweep rates.

To enhance understanding, eqn (10) was modified as follows:

$$\frac{i(\upsilon)}{\upsilon^{1/2}} = \frac{k_1}{\upsilon^{1/2}} + k_2 \qquad (11)$$

In eqn (11), $k_1\upsilon$ and $k_2\upsilon^{1/2}$ are the current contributions from the surface capacitive and diffusion-controlled intercala-

tion processes, respectively. Therefore, by determining k_1 and k_2 from the slope and intercept of the y-axis from linear regression, we are able to measure their contribution to the current density at the fixed specific potential.[91]

The usual curve $\{(V)/\upsilon^{1/2}$ vs. $\upsilon^{1/2}\}$ in Fig. 6c represents the contribution of surface-mediated capacitance and diffusion-controlled intercalation processes at different scan rates.

Specific contribution at a 10 mV s^{-1} scan rate is shown in Fig. 6d. Surface capacitance or electrosorption was found to contribute 46.0%, whereas diffusion-controlled intercalation contributed around 54.0%. The amount of charge stored in the outer and inner surfaces was also determined using the Trasatti plot. The total specific capacitance of the electrode, according to Trassati, is influenced by both the inner and outer surface capacitances. This can be expressed as:

$$C_{Total} = C_{in} + C_{out} \tag{12}$$

The charge storage mechanism depends on the scan rate used in the study of CV. The y-intercept in Fig. 6e represents the capacitance, which indicates the overall charge storage capacity of the electrode. This is determined by plotting the linear fit of C^{-1} *vs.* $v^{1/2}$ at different scan rates. The outer surface capacitance or charge storage of the electrode is represented by the y-intercept in Fig. 6f, which illustrates the linear fit of C *vs.* $v^{-1/2}$. C_{in}'s measured value was 1337.5 F g^{-1}, accounting for 56% of the overall capacitance value. Similarly, C_{out} was estimated to be 1049 F g^{-1}, representing 44% of the overall capacitance value. The total capacitance value (C_{total}) was determined to be 2386.5 F g^{-1}. This confirms that the charge storage or capacitance of the Ni$_{0.5}$Co$_{0.5}$S electrodes is a combination of redox-mediated diffusion-controlled intercalating process and surface absorption processes.

To better understand the electrochemical characteristics of charge storage of the Ni$_{0.5}$Co$_{0.5}$S electrode, galvanostatic charge–discharge (GCD) studies in 4 M KOH aqueous electrolytes were performed. The electrode's specific capacitance can be determined by analysing the charge–discharge curve using eqn (13).[71,91]

$$C_{sp} = \frac{I\Delta t}{m\Delta V} \tag{13}$$

The calculation of the electrode's specific capacity in mA h g^{-1} requires the modification of eqn (13) as follows:

$$C(\text{mA h g}^{-1}) = C_{sp}\Delta V/3.6 = \frac{I\Delta t}{m \times 3.6} \tag{14}$$

where C_{sp} is the specific capacitance in F g^{-1}, potential window in the charge–discharge measurement ΔV (V), discharge current density I (A), discharge time Δt (s), and m is the loading mass of the active material in the electrode (g).

Fig. 7a displays the galvanostatic specific capacity/capacitances corresponding to 1, 2, 3, 5, and 10 A g^{-1} current densities, measured as 267, 221.3, 191.2, 155.8, and 95.5 mA h g^{-1} (1920, 1593.4, 1376.6, 1121.7, 687.6 F g^{-1}), respectively. The GCD, as mentioned above, showed that as the current density increases, the specific capacitance gradually decreases. The stability of the electrode is shown in Fig. 7b (capacitance value *vs.* cycle number at different current densities). The Ni$_{0.5}$Co$_{0.5}$S electrode's long-term cycling stability at 10 A g^{-1} for 10 000 cycles is shown in Fig. 7c resulting in 84.0% capacity retention. The electrode's specific capacitance did not vary significantly from its initial capacitance after 10 000 cycles. After continuous charge/discharge of 10 000 cycles, the electrode's coulom-

bic efficiency $\left(\eta = \frac{t_d}{t_c}\right)$ was 92.2%, demonstrating the outstanding reversibility of the Ni$_{0.5}$Co$_{0.5}$S electrode. The comparison of galvanostatic specific capacitance in mA h g^{-1} at 1, 2, and 4 M KOH concentrations is shown in Fig. 7d. At a current density of 1 A g^{-1}, the electrode demonstrates a higher specific capacitance in 4 M KOH electrolyte (with an extended discharge time) compared to 1 and 2 M KOH electrolytes. From the GCD experiment, the charge storage capacity (more realistic and applicable capacitance) of the electrode was measured using eqn (13) and (14), which are 214.8, 243.8, and 267 mA h g^{-1} (1547, 1756, and 1920 F g^{-1}) for concentrations of 1, 2, and 4 M KOH electrolyte, respectively. The comparative specific capacitance observations confirmed an increase in specific capacitance value from 1 M to 4 M KOH concentration, which is similar to the findings of the CV results.

The electrochemical impendence spectra (EIS) were studied (before and after 10 000 repeated charge–discharge cycles) to evaluate the electrode kinetics and interface resistance at an open circuit potential in the frequency range of 100 kHz to 0.1 Hz. The impedance characteristic as a function of frequency is depicted in the Nyquist plot (Fig. 7e). This plot can be divided into two distinct sections. Firstly, there is a depressed arc observed in the high-frequency region, corresponding to the faradaic responses. Secondly, a straight line is observed in the low-frequency region, indicating a rapid OH$^-$ ion diffusion-controlled process. Furthermore, the impedance contribution was ascribed to the impedance distributions across internal series resistance (R_s), charge transfer resistance (R_{ct}), and Warburg impedance (R_w). The internal series resistance (R_s) is represented by the point at which the curve intersects the real axis in the high-frequency region, which includes the resistance of the active material, electrolyte, and connected wires at the electrode–electrolyte interface. The Ni$_{0.5}$Co$_{0.5}$S electrode has R_s and R_{ct} values of 1.01 and 0.72, respectively. The lower-frequency data provide insights into the Warburg diffusion resistance shown by the Ni$_{0.5}$Co$_{0.5}$S electrode.[92] Based on the EIS spectra, the Ni$_{0.5}$Co$_{0.5}$S electrode shows good electrochemical stability after 10 000 consecutive charge–discharge cycles compared to the initial. The phase angle of the electrode concerning the applied frequency is seen in Fig. 7f of the Bode plot. The Ni$_{0.5}$Co$_{0.5}$S electrode's phase angles were 52.2° at the beginning and 45.48° at the end of 10 000 cycles, respectively. The confirmation of the pseudocapacitive charge storage capacity of the Ni$_{0.5}$Co$_{0.5}$S electrode is shown by observing a reduced phase angle (about 50°), consistent with the findings depicted in the Nyquist plot.[4,93] After 10 000 charge–discharge cycles, the active electrode material of Ni$_{0.5}$Co$_{0.5}$S was extracted from the electrode and examined by powder XPS, Raman spectroscopy, and XRD to further investigate the long-term structural stability of the Ni$_{0.5}$Co$_{0.5}$S electrode during electrochemical testing. The inset in Fig. S1c† shows the Raman spectrum of the Ni$_{0.5}$Co$_{0.5}$S electrode after a continuous charge–discharge experiment. It shows peaks at 150.6, 394.5, 467, 513 and 635 cm^{-1} which can be indexed to the Raman-active vibrational peaks of the Ni$_{0.5}$Co$_{0.5}$S sample, which correspond to the typical phonon modes F$_{2g}$, E$_g$, T$_{2g}$ and A$_{1g}$ respectively.
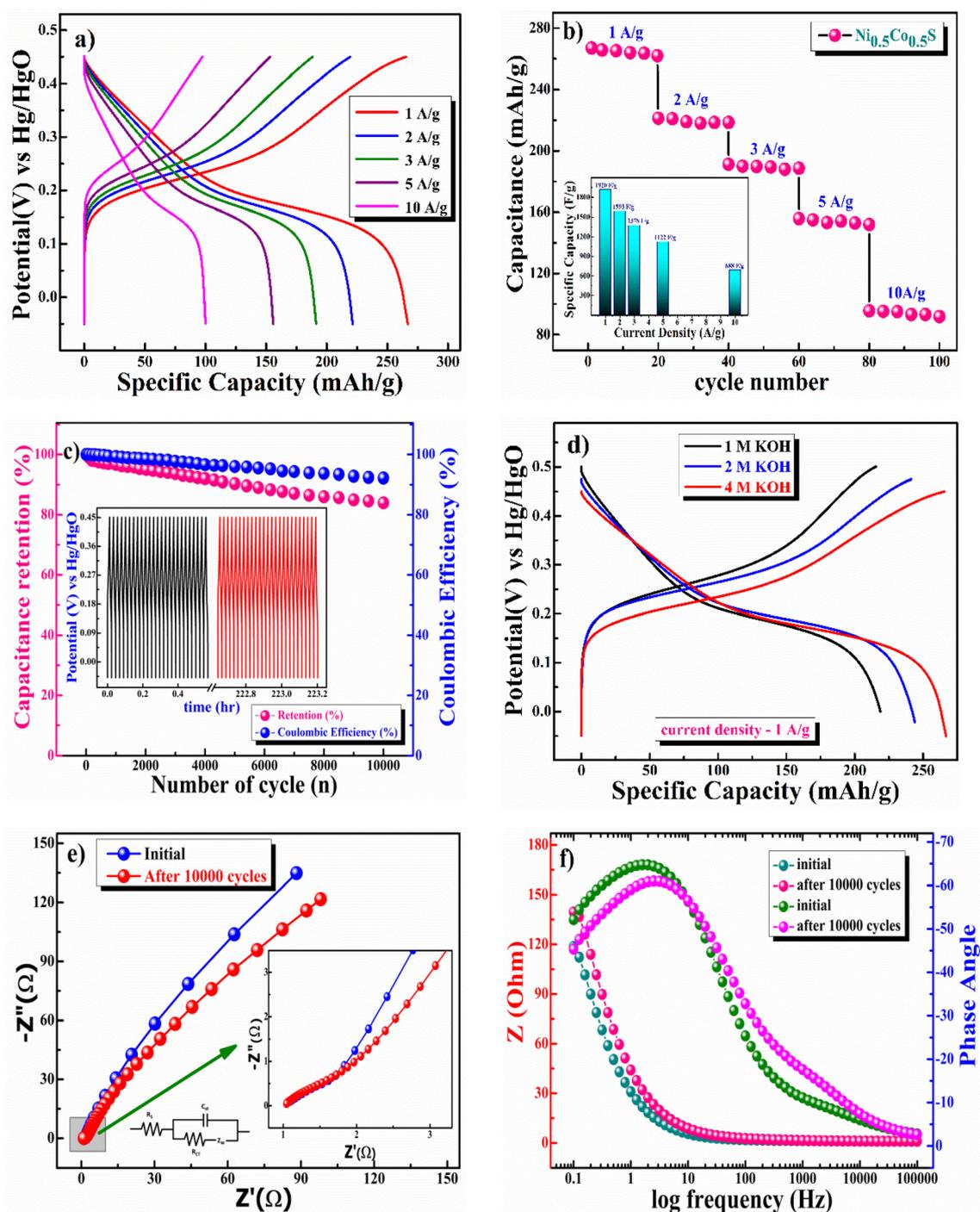
Fig. 7 (a) The galvanostatic charge/discharge graph for the $Ni_{0.5}Co_{0.5}S$ electrode, (b) $Ni_{0.5}Co_{0.5}S$ electrode capacitance performance at different constant current rates, (c) coulombic efficiency and capacitance retention of the $Ni_{0.5}Co_{0.5}S$ electrode, (d) the comparison of GCD at concentrations of 1, 2, and 4 M KOH, (e and f) Impedance spectra for the $Ni_{0.5}Co_{0.5}S$ electrode are shown in the Nyquist and Bode plot at 10 mV between 100 kHz to 0.1 Hz.

The two A_{1g} modes (150.6 and 635 cm^{-1}) can be attributed to the stretching of the S atom in the S–M–S (M = Ni & Co) bond. The XPS spectra shown in ESI Fig. S3† reflect the electrochemical processes and the reversible conversion of the elemental states of Ni and Co during charge and discharge, contributing to higher capacitance. The binding energy is shifted to a lower value which can be attributed to the accumulation of charge at the electrode surface which is often associated with the adsorption of species or the formation of an electrical double layer. Fig. S4† shows the XRD spectra after continuous charge–discharge, indicating that the crystal structure of the electrode has led to a very small deterioration in the per-

formance after continuous charge–discharge experiments as there is no change in the crystal structure of the electrode and the crystal structure of the parent $Ni_{0.5}Co_{0.5}S$ remains intact even after 10 000 charge–discharge cycles.[94–96]

The charge storage behaviour of $Ni_{0.5}Co_{0.5}S$ electrodes was also investigated in a neutral 0.5 M Na_2SO_4 electrolyte. ESI Fig. S5a† shows well-separated redox peaks in the CV curve at various scan speeds (+0.64/+0.52 V at 1 mV s^{-1} scan rate). For the $Ni_{0.5}Co_{0.5}S$ electrode in 0.5 M Na_2SO_4 electrolyte, the calculated specific capacitance (which depends on the scan rate) was found to be 414.4, 290, 207.5, 140, 95.6, and 82.8 F g^{-1} for the scan rates of 1, 5, 10, 40, 80, and 100 mV s^{-1} respectively. The quantitative GCD measurements findings are shown in ESI Fig. S5b,† and values were found to be 57, 43, 33.3, 19.3, and 9 mA h g^{-1} (410.4, 309.6, 239.8, 138.9, and 64.8 F g^{-1}) at the current density of 1, 2, 3, 5, and 10 A g^{-1}, respectively.

Additionally, a comparative study compared the effects of the anion on the electrolyte between 0.5 M Na_2SO_4 and 4 M KOH. The $Ni_{0.5}Co_{0.5}S$ electrode's comparative CV curve in 0.5 M Na_2SO_4 and 4 M KOH electrolytes is shown in ESI Fig. S5c.† There were observed shifts in the position of the redox peaks while transitioning from an OH electrolyte to a Na_2SO_4 electrolyte. Additionally, it was found that the redox peaks in 4 M KOH were more dominant than those in 0.5 M Na_2SO_4; this could be due to the size difference between the hydration radii of sulfate ions (3.79 Å) and hydroxyl ions (3 Å). The larger size of SO_4^{2-} results in slow kinetics in diffusion-controlled processes resulting in lower charge storage in the neutral Na_2SO_4 electrolyte. Furthermore, the current response of the CV curve may be attributed to the greater molar conductance of OH$^-$ ions (198 cm^2 Ω mol^{-1}) in the KOH electrolyte, as compared to the conductivity of SO_4^{2-} ions (79.8 cm^2 Ω mol^{-1}) in Na_2SO_4.[80,84] GCD studies in 0.5 M Na_2SO_4 and 4 M KOH electrolytes were used to evaluate the electrode's capacitance quantitatively. In 4 M KOH compared to the 0.5 M Na_2SO_4 electrolyte, the electrode provides a greater specific capacitance value (longer discharge time), as illustrated in ESI Fig. S5d.† These investigations confirm the excellent electrode performance of the electrode in aqueous KOH electrolyte.

Two electrode full cell test in asymmetric supercapacitor cell (ASC) mode

To explore the real applicability of the $Ni_{0.5}Co_{0.5}S$ electrode, the two-electrode full cell was fabricated in ASC mode in a 4 M KOH electrolyte where AC was employed as a counter electrode. The storage capacities of the positive and negative electrodes must be balanced using eqn (15) to estimate the maximum specific capacitance during the full-cell test.

$$\frac{1}{C_{total}} = \frac{1}{C_{positive}} + \frac{1}{C_{negative}} \tag{15}$$

To balance the cell's capacity to store charges, eqn (16) was used to calculate the mass ratio (m^+/m^-) of the materials of an individual electrode that make up the positive and negative electrodes.

$$\frac{m^+}{m^-} = \frac{C_- \times \Delta E_-}{C_+ \times \Delta E_+} \tag{16}$$

where C_+, C_-, m^+, m^-, ΔE_+, and ΔE_- are estimates of the specific capacitance, mass loading on the electrode, and potential window of positive and negative electrodes based on measurements made with a single electrode.[41,91]

With a fixed scan rate (10 mV s^{-1}), separate CV curves for $Ni_{0.5}Co_{0.5}S$ (positive electrode) and AC (negative electrode) are shown in Fig. 8a with a single operating potential window range. In the ESI (Fig. S6 and S7†), the electrochemical properties of the constructed AC electrode are shown using CV and GCD. The specific capacitance of the AC electrode was 96.4 mA h g^{-1} (347 F g^{-1}) at 1 A g^{-1} from the GCD experiment and 91.3 mA h g^{-1} (328.5 F g^{-1}) at a scan rate of 1 mV s^{-1} in CV. Because AC is employed to improve the conductivity of the active electrode, the contribution to capacitance caused by the AC electrode is subtracted when determining the $Ni_{0.5}Co_{0.5}S$ electrode's electrochemical charge storage capacity. Thus, the acquired data solely displays the $Ni_{0.5}Co_{0.5}S$ electrode's capacitive value. The calculated mass ratio ($m+/m$) for the asymmetric cell was 1.0 : 3.6, while the active material's weight was found to be 4.0 mg (activated carbon and PVDF weights excluded).

Two-electrode $Ni_{0.5}Co_{0.5}S$//AC, asymmetric supercapacitor cells (ASCs), are shown in Fig. 8b with their CV plots at scan rates ranging from 1 to 100 mV s^{-1} in the potential window 0 to 1.5 V. The GCD plot of the full cell at various current densities is shown in Fig. 8c. At constant current densities of 1, 2, 3, 5, and 10 A g^{-1}, the specific capacitances of ASCs derived from GCD curves were 254, 202.8, 173.8, 149.7, and 106.5 mA h g^{-1} (609.6, 487, 417, 359.3, and 255.6 F g^{-1}), respectively. The EIS (Nyquist and Bode) plots at an open circuit potential in the 100 kHz to 0.1 Hz frequency range are shown in Fig. 8d and e, confirming the superior charge transfer, higher specific capacitance, and excellent retention of the electronic structure of the $Ni_{0.5}Co_{0.5}S$ electrode//AC full cell in ASC mode.

However, a slight reduction in capacity is due to the partially irreversible nature of the electrode, which was observed during the cycling test. The EIS result supports the evidence for cycling stability by displaying a slight variation in the cell's internal and charge transfer resistances before and after the cycling test.

The $Ni_{0.5}Co_{0.5}S$ electrode//AC full cell, as shown in Fig. 8f, has exceptional long-term cycling stability, with 89.5% capacity retention after 10 000 cycles. Furthermore, after 10 000 cycles, the $Ni_{0.5}Co_{0.5}S$ electrode//AC full cell's coulombic efficiency has decreased by merely 5% from its initial value.

Eqns (17) and (18) were utilized to calculate the power and energy density of the ASC.

$$P(\text{W kg}^{-1}) = \frac{E \times 3600}{t_{dis}} \tag{17}$$

$$E(\text{W h kg}^{-1}) = \frac{1}{2}\frac{C_{ASC}}{3.6}\Delta V^2 \tag{18}$$

where ΔV is the operating voltage window, C_{sp} is the specific capacitance, and t_{dis} is the discharge time. Fig. 8g compares
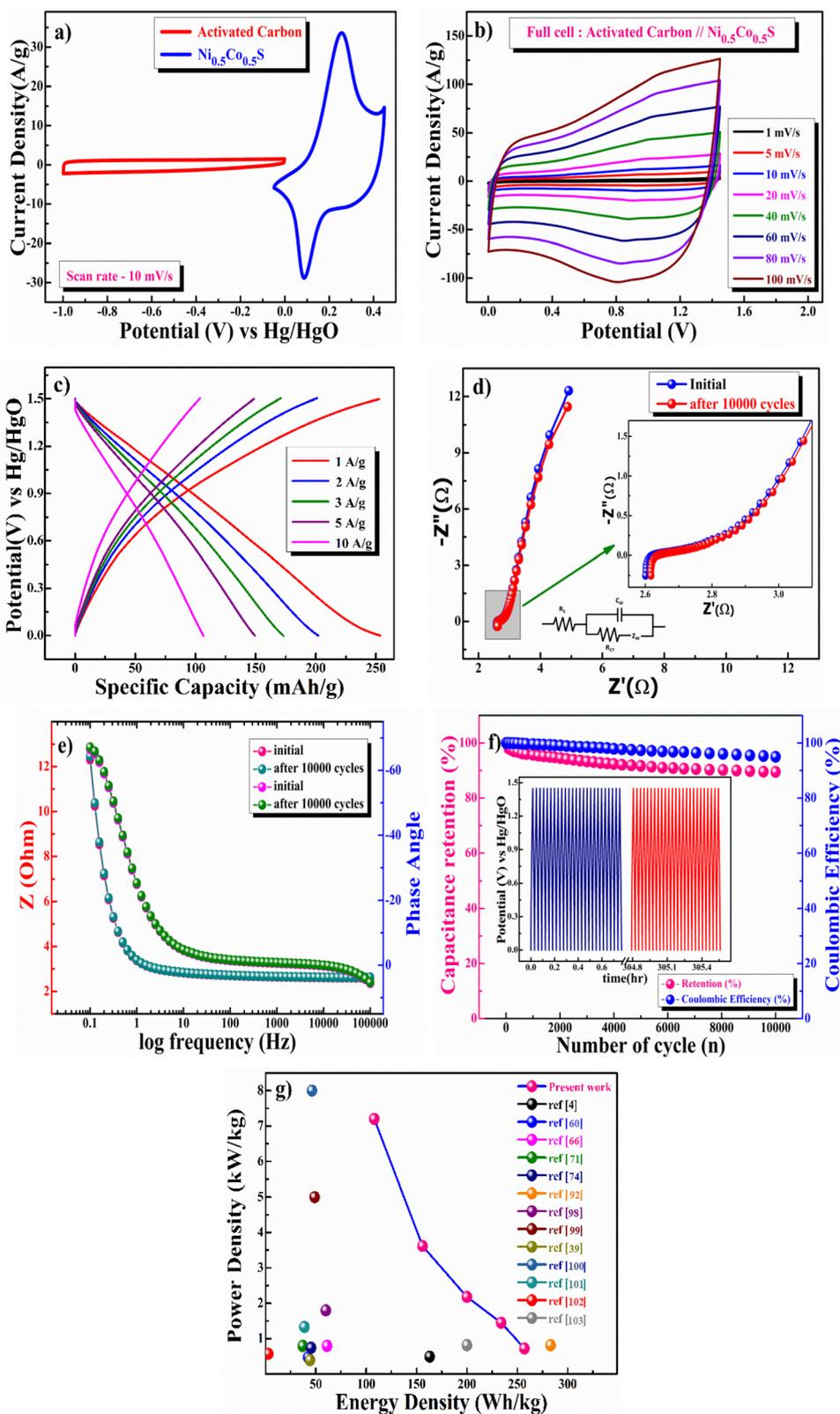
Fig. 8 (a) Separate CV plots for the activated carbon and the $Ni_{0.5}Co_{0.5}S$ electrode in a 4 M KOH electrolyte, (b) CV plots at various sweep rates; (c) charging and discharging at various current densities, (d) Nyquist and (e) Bode diagram at the beginning of the cycle and after 10 000 cycles at 10 mV^{-1} of the ASC full cell, (f) coulombic efficiency and capacitance retention, and (g) a Ragone plot comparing the $Ni_{0.5}Co_{0.5}S$//AC full cell in the ASC mode with established supercapacitor devices.

Table 1 Compares the $Ni_{0.5}Co_{0.5}S$ electrode//AC (ASC) full-cell Ragone plot with known supercapacitor devices

Material	Energy density (W h kg^{-1})	Power density (kW kg^{-1})	Cycling stability (%) after "n" cycles	Capacitance (3 electrode system)	Electrolyte solution	Ref.
β-NiS	163	0.5	90.0%, 2500	1578 F g^{-1} at 1 A g^{-1}	2 M KOH	4
$NiCo_2S_4$ hollow spheres	42.3	0.48	78.6%, 10 000	1036 F g^{-1} at 1 A g^{-1}	6 M KOH	60
$Ni_{1.5}Co_{1.5}S_4$@CNTs	61.2	0.8	91.5% 10 000	210 mA h g^{-1} at 1 A g^{-1}	2 M KOH	66
$(Co_{0.5}Ni_{0.5})_9S_8$/N-C	—	—	83%, 100	723.7 A h g^{-1} at 1 A g^{-1}	1 M $NaClO_4$ in (PC + FEC)	70
$mNi_{0.32}Co_{0.68}S_2$	37	0.8	66.0%, 1000	1698 F g^{-1} at 2 A g^{-1}	2 M KOH	71
$Ni_xCo_{1-x}S$@C-3	45.31	0.75	91.0%, 8000	709 C g^{-1} at 1 A g^{-1}	6 M KOH	73
$Co_{0.5}Ni_{0.5}C_2O_4$	283	0.82	90.7%, 2500	2396 F g^{-1} at 1 A g^{-1}	2 M KOH	91
Ni-Co-S$_4$ nanosheets	60	1.8	90.1%, 10 000	1285 F g^{-1} at 100 A g^{-1}	1 M KOH	97
Mn incorporated MoS_2	48.8	5.0	77.0%, 5000	430 F g^{-1} at 5 mV s^{-1}	0.5 M Na_2SO_4	98
CoS-AC//AC	44.2	0.4	77.5%, 2000	797.79 F g^{-1} at 10 A g^{-1}	$K_3Fe(CN)_6$ + KOH	39
FeCo-A-S	46.1	8.0	79.3%, 10 000	2932.2 F g^{-1} at 1 A g^{-1}	3 M KOH	99
3D $NiCo_2S_4$ nanostructure	38.64	1.33	72.7%, 10 000	2363.1 F g^{-1} at 2.5 A g^{-1}	6 M KOH	100
Ni_3S_2/NF	2.93	0.38	81.25%, 6000	255.3 mA h g^{-1} at 3 A g^{-1}	1 M KOH	101
$KNiPO_4$	200	0.82	92.3%, 2200	168.5 mA h g^{-1} at 1 A g^{-1}	2 M KOH	102
$SnS-SnS_2$@GO	—	—	69.8%, 100	450.6 mA h g^{-1} at 0.1 A g^{-1}	1 M $NaClO_4$ in (EC + DMC + MEC)	103
$Ni_{0.5}Co_{0.5}S$ nano-chains	**257**	**0.73**	**89.5%, 10 000**	**267 mA h g^{-1} at 1 A g^{-1}**	**4 M KOH**	**Present work**

the Ragone plot (energy density *vs.* power density) of the $Ni_{0.5}Co_{0.5}S$ electrode//AC full-cell with those of previously reported supercapacitors made of nickel, cobalt, and sulfur. At 1 A g^{-1} current density, the ASC's results demonstrated a significant power density of 0.73 kW kg^{-1}, and the highest energy density of 257.0 W h kg^{-1}. When the current density was increased to 10 A g^{-1}, the energy density decreased to 108.0 W h kg^{-1}, yielding a maximum power density of 7.20 kW kg^{-1}. For comparison, the specific capacitance, capacity retention, energy density, and power density of different sulfide-based electrodes for supercapacitor applications are presented in Table 1 and it confirms that $Ni_{0.5}Co_{0.5}S$ nano-chains showed superior or at least comparable electrode performances to other sulfide based electrodes.

This suggests that a predominant redox-mediated diffusion-controlled pseudocapacitive mechanism in combination with surface capacitance (electrosorption) is the cause of the materials' high charge storage capacity. An optimal energy density of 257.0 W h kg^{-1} and a power density of 0.73 kW kg^{-1} were attained by the $Ni_{0.5}Co_{0.5}S$//AC full cell in the 1.5 V voltage window with a 4 M KOH electrolyte at a current rate of 1 A g^{-1}. The study suggests that the capacitance value and charge storage characteristics are better or on par with most previously reported transition-metal sulfide nanostructured pseudocapacitors and supercapacitors. These findings demonstrate the potential of $Ni_{0.5}Co_{0.5}S$ nano-chains as a pseudocapacitive electrode for large-scale energy storage applications.

Conclusions

In summary, single-phase hexagonal $Ni_{0.5}Co_{0.5}S$ nano-chains consisting of interconnected nano-spheres were synthesized using a simple H_2S-mediated heterogeneous two-phase (gas diffusion in liquid) precipitation route in an aqueous medium. $Ni_{0.5}Co_{0.5}S$ nano-chains developed in a single phase due to the controlled precipitation of the solid phase caused by the slow diffusion of H_2S gas into the liquid phase. The XRD pattern confirmed the single-phase hexagonal $Ni_{0.5}Co_{0.5}S$ nano-crystalline material, and the average crystallite size, as determined by the Debye–Scherrer equation, was around 21 nm. The nano-chain structure may provide rapid electron transport inside the material for a high/fast rate of electrochemical charge storage/capacitance of the materials. Having a specific capacitance between −0.05 and 0.45 V of 2001.6 F g^{-1} at 1 mV s^{-1} in CV and 267 mA h g^{-1} (1920 F g^{-1}) at 1 A g^{-1} in the GCD experiment, the $Ni_{0.5}Co_{0.5}S$ electrode demonstrated an excellent pseudocapacitive charge storage performance. Furthermore, the surface (outer) and intercalative (inner) charges stored by the $Ni_{0.5}Co_{0.5}S$ electrodes were 46.0%, and 54.0%, respectively.

Conflicts of interest

No conflicts of interest are disclosed by the authors.

Acknowledgements

References

1 Y. Jiang and J. Liu, Definitions of Pseudocapacitive Materials: A Brief Review, *Energy Environ. Mater.*, 2019, **2**, 30–37.

2 M. Y. Worku, Recent Advances in Energy Storage Systems for Renewable Source Grid Integration: A Comprehensive Review, *Sustainability*, 2022, **14**, 5985.

3 X. He and X. Zhang, A comprehensive review of supercapacitors: Properties, electrodes, electrolytes and thermal management systems based on phase change materials, *J. Energy Storage*, 2022, **56**, 106023.

4 V. Kushwaha, A. Gupta, R. B. Choudhary, K. D. Mandal, R. Mondal and P. Singh, Nanocrystalline β-NiS; A Redox-mediated Electrode in Aqueous Electrolyte for Pseudo-capacitor/Supercapacitor Applications, *Phys. Chem. Chem. Phys.*, 2023, **25**, 555.

5 P. Simon and Y. Gogotsi, Materials for electrochemical capacitors, *Nat. Mater.*, 2008, **7**, 845–854.

6 M. Winter and R. J. Brodd, What Are Batteries, Fuel Cells, and Supercapacitors?, *Chem. Rev.*, 2004, **104**, 4245–4269.

7 S. Balasubramaniam, A. Mohanty, S. K. Balasingam, S. J. Kim and A. Ramadoss, Comprehensive Insight into the Mechanism, Material Selection and Performance Evaluation of Supercapatteries, *Nano-Micro Lett.*, 2020, **12**, 1–46.

8 L. Yu and G. Z. Chen, Supercapatteries as High-Performance Electrochemical Energy Storage Devices, *Electrochem. Energy Rev.*, 2020, **3**, 271–285.

9 L. Yu and G. Z. Chen, Redox electrode materials for super-capatteries, *J. Power Sources*, 2016, **326**, 604–612.

10 M. E. Sahin, F. Blaabjerg and A. Sangwongwanich, A Comprehensive Review on Supercapacitor Applications and Developments, *Energies*, 2022, **15**, 674.

11 S. Cheng, Y. Zhang, Y. Liu, Z. Sun, P. Cui, J. Zhang, X. Hua, Q. Su, J. Fu and E. Xie, Energizing Fe_2O_3-based supercapacitors with tunable surface pseudocapacitance *via*, physical spatial-confining strategy, *Chem. Eng. J.*, 2021, **406**, 126875.

12 Y. Xiang, Z. Yang, S. Wang, M. S. A. Hossain, J. Yu, N. A. Kumar and Y. Yamauchi, Pseudocapacitive behavior of the Fe_2O_3 anode and its contribution to high reversible capacity in lithium ion batteries, *Nanoscale*, 2018, **10**, 18010.

13 M. Jia, T. Qi, Q. Yuan, P. Zhao and M. Jia, Polypyrrole Modified MoS_2 Nanorod Composites as Durable Pseudocapacitive Anode Materials for Sodium-Ion Batteries, *Nanomaterials*, 2022, **12**, 2006.

14 T. Yao, M. Yao and H. Wang, Porous graphene-like MoS_2/carbon hierarchies for high-performance pseudo-capacitive sodium storage, *Sustainable Energy Fuels*, 2022, **6**, 822.

15 P. Man, Q. Zhang, Z. Zhou, M. Chen, J. Yang, Z. Wang, Z. Wang, B. He, Q. Li, W. Gong, W. Lu, Y. Yao and L. Wei, Engineering MoS_2 Nanosheets on Spindle-Like α-Fe_2O_3 as High-Performance Core-Shell Pseudocapacitive Anodes for Fiber-Shaped Aqueous Lithium-Ion Capacitors, *Adv. Funct. Mater.*, 2020, **30**, 2003967.

16 M. Mirzaeian, N. Akhanova, M. Gabdullin, Z. Kalkozova, A. Tulegenova, S. Nurbolat and K. Abdullin, Improvement of the Pseudocapacitive Performance of Cobalt Oxide-Based Electrodes for Electrochemical Capacitors, *Energies*, 2020, **13**, 5228.

17 J. Li, G. Zanab and Q. Wu, An ultra-high-performance anode material for supercapacitors: self-assembled long Co_3O_4 hollow tube network with multiple heteroatom (C-, N- and S-) doping, *J. Mater. Chem. A*, 2016, **4**, 9097.

18 D. Yan, Y. Huang, Y. Yua and G. Cao, β-$NaVO_3$ as a pseudocapacitive anode material for sodium-ion batteries, *New J. Chem.*, 2023, **47**, 1268.

19 S. J. Patil, N. R. Chodankar, Y. K. Han and D. W. Lee, Carbon alternative pseudocapacitive V_2O_5 nanobricks and δ-MnO_2 nanoflakes @ α-MnO_2 nanowires hetero-phase for high-energy pseudocapacitor, *J. Power Sources*, 2020, **453**, 227766.

20 S. Fu, Q. Yu, Z. Liu, P. Hu, Q. Chen, S. Feng, L. Mai and L. Zhou, Yolk-shell Nb_2O_5 microspheres as intercalation pseudocapacitive anode materials for high-energy Li-ion capacitors, *J. Mater. Chem. A*, 2019, **7**, 11234.

21 N. Zhaoa, H. Fana, M. Zhanga, J. Maa, Z. Dua, B. Yana, H. Lia and X. Jiang, Simple electrodeposition of MoO_3 film on carbon cloth for high-performance aqueous symmetric supercapacitors, *Chem. Eng. J.*, 2020, **390**, 124477.

22 L. Xu, W. Zhou, S. Chao, Y. Liang, X. Zhao, C. Liu and J. Xu, Advanced Oxygen-Vacancy Ce-Doped MoO_3 Ultrathin Nanoflakes Anode Materials Used as Asymmetric Supercapacitors with Ultrahigh Energy Density, *Adv. Energy Mater.*, 2022, **12**, 2200101.

23 N. Naresh, P. Jena and N. Satyanarayana, Facile synthesis of MoO_3/rGO nanocomposite as anode materials for high performance lithium-ion battery applications, *J. Alloys Compd.*, 2019, **810**, 151920.

24 N. Jabeen, Q. Xia, S. V. Savilov, S. M. Aldoshin, Y. Yu and H. Xia, Enhanced Pseudocapacitive Performance of α-MnO_2 by Cation Preinsertion, *ACS Appl. Mater. Interfaces*, 2016, **8**, 33732–33740.

25 P. Geng, S. Zheng, H. Tang, R. Zhu, L. Zhang, S. Cao, H. Xue and H. Pang, Transition Metal Sulfides Based on Graphene for Electrochemical Energy Storage, *Adv. Energy Mater.*, 2018, **8**, 1703259.

26 W. Liu, H. Niu, J. Yang, K. Cheng, K. Ye, K. Zhu, G. Wang, D. Cao and J. Yan, Ternary Transition Metal Sulfides Embedded in Graphene Nanosheets as Both the Anode and Cathode for High-Performance Asymmetric Supercapacitors, *Chem. Mater.*, 2018, **30**, 1055–1068.

27 C. K. Kanade, H. Seok, V. K. Kanade, K. Aydin, H. U. Kim, S. B. Mitta, W. J. Yoo and T. Kim, Low-Temperature and Large-Scale Production of a Transition Metal Sulfide Vertical Heterostructure and Its Application for Photodetectors, *ACS Appl. Mater. Interfaces*, 2021, **13**, 8710–8717.

28 P. Wang, D. Wu, K. Zhang and X. Wu, Two-Dimensional Quaternary Transition Metal Sulfide $CrMoA_2S_6$ (A = C, Si, or Ge): A Bipolar Antiferromagnetic Semiconductor with a High Néel Temperature, *J. Phys. Chem. Lett.*, 2022, **13**, 3850–3856.

29 Q. Zhu, Q. Xu, M. Du, X. Zeng, G. Zhong, B. Qiu and J. Zhang, Recent Progress of Metal Sulfide Photocatalysts

for Solar Energy Conversion, *Adv. Mater.*, 2022, **34**, 2202929.

30 J. Chen, D. H. C. Chua and P. S. Lee, The Advances of Metal Sulfides and In Situ Characterization Methods beyond Li Ion Batteries: Sodium, Potassium, and Aluminum Ion Batteries, *Small Methods*, 2020, **4**, 1900648.

31 J. Rehman, K. Eid, R. Ali, X. Fan, G. Murtaza, M. Faizan, A. Laref, W. Zheng and R. S. Varma, Engineering of Transition Metal Sulfide Nanostructures as Efficient Electrodes for High-Performance Supercapacitors, *ACS Appl. Energy Mater.*, 2022, **5**, 6481–6498.

32 O. Ola and K. Thummavichai, Layered tungsten-based composites and their pseudocapacitive and electro-catalytic performance, *Mater. Chem. Front.*, 2022, **6**, 737–747.

33 A. D. Adhikari, S. Singh and I. Lahiri, WS₂@PPy hetero-structured high performance supercapacitor self-powered by PVDF piezoelectric separator, *J. Alloys Compd.*, 2023, **939**, 168713.

34 V. Shrivastav, S. Sundriyal, V. Shrivastav, U. K. Tiwari and A. Deep, WS₂/Carbon Composites and Nanoporous Carbon Structures Derived from Zeolitic Imidazole Framework for Asymmetrical Supercapacitors, *Energy Fuels*, 2021, **35**, 15133–15142.

35 J. Chen, X. Zhou, C. Mei, J. Xu, S. Zhou and C. P. Wong, Pyrite FeS₂ nanobelts as high-performance anode material for aqueous pseudocapacitor, *Electrochim. Acta*, 2016, **222**, 172–176.

36 X. Xu, L. Li, H. Chen, X. Guo, Z. Zhang, J. Liu, C. Mao and G. Li, Constructing heterostructured FeS₂/CuS nano-spheres as high rate performance lithium ion battery anodes, *Inorg. Chem. Front.*, 2020, **7**, 1900.

37 Y. Hu and L. Zhang, Boosting High-Rate Sodium Storage of CuS via a Hollow Spherical Nanostructure and Surface Pseudocapacitive Behavior, *ACS Appl. Energy Mater.*, 2021, **4**, 8901–8909.

38 R. Li, J. Tian, W. Wu, Q. Wang, C. Zhang, C. Zhou and L. Yang, CuS/polyaniline nanoarray electrodes for appli-cation in high-performance flexible supercapacitors, *J. Energy Storage*, 2022, **55**, 105385.

39 T. Xu, Z. Wang, G. Wang, L. Lu, S. Liu, S. Gao, H. Xu and Z. Yu, One-pot synthesis of a CoS-AC electrode in a redox electrolyte for high-performance supercapacitors, *J. Appl. Electrochem.*, 2019, **49**(11), 1069–1077.

40 P. Justin and G. R. Rao, CoS spheres for high-rate electro-chemical capacitive energy storage application, *Int. J. Hydrogen Energy*, 2010, **35**, 9709–9715.

41 K. Subramani, N. Sudhan, R. Divya and M. Sathish, All-solid-state asymmetric supercapacitors based on cobalt hexacyanoferrate-derived CoS and activated carbon, *RSC Adv.*, 2017, **7**, 6648–6659.

42 N. Arsalani, L. S. Ghadimi, I. Ahadzadeh, A. G. Tabrizi and T. Nann, Green Synthesized Carbon Quantum Dots/ Cobalt Sulfide Nanocomposite as Efficient Electrode Material for Supercapacitors, *Energy Fuels*, 2021, **35**, 9635–9645.

43 B. Qu, Y. Chen, M. Zhang, L. Hu, D. Lei, B. Lu, Q. Li, Y. Wang, L. Chen and T. Wang, β-Cobalt sulfide nano-particles decorated graphene composite electrodes for high capacity and power supercapacitors, *Nanoscale*, 2012, **4**, 7810–7816.

44 T. Zhu, Z. Wang, S. Ding, J. Chen and X. W. Lou, Hierarchical nickel sulfide hollow spheres for high per-formance supercapacitors, *RSC Adv.*, 2011, **1**, 397–400.

45 J. Yang, X. Duan, W. Guo, D. Li, H. Zhang and W. Zheng, Electrochemical performances investigation of NiS/rGO composite as electrode material for supercapacitors, *Nano Energy*, 2014, **5**, 74–81.

46 X. Lei, M. Li, M. Lu and X. Guan, Electrochemical Performances Investigation of New Carbon-Coated Nickel Sulfides as Electrode Material for Supercapacitors, *Materials*, 2019, **12**, 3509.

47 P. Gaikar, S. P. Pawar, *et al.*, Synthesis of nickel sulfide as a promising electrode material for pseudocapacitor appli-cation, *RSC Adv.*, 2016, **6**, 112589–112593.

48 H. Wang, J. Wang, M. Liang, *et al.*, Novel Dealloying-Fabricated NiS/NiO Nanoparticles with Superior Cycling Stability for Supercapacitors, *ACS Omega*, 2021, **6**, 17999–18007.

49 Y. J. Lee, B. S. Reddy, H. A. Hong, K. W. Kim, S. J. Cho, H. J. Ahn, J. H. Ahn and K. K. Cho, Synthesis and electro-chemical properties of nickel sulfide/carbon composite as anode material for lithium-ion and sodium-ion batteries, *Int. J. Energy Res.*, 2022, **46**, 16883–16895.

50 N. Feng, D. Hu, P. Wang, X. Sun, X. Li and D. He, Growth of nanostructured nickel sulfide films on Ni foam as high-performance cathodes for lithium ion batteries, *Phys. Chem. Chem. Phys.*, 2013, **15**, 9924.

51 X. Zhang, Y. Zhao, C. Zhang, C. Wu, X. Li, M. Jin, W. Lan, X. Pan, J. Zhou and E. Xie, Cobalt sulfide embedded carbon nanofibers as a self-supporting template to improve lithium ion battery performances, *Electrochim. Acta*, 2021, **366**, 137351.

52 B. Wang, Y. Cheng, H. Su, M. Cheng, Y. Li, H. Geng and Z. Dai, Boosting Transport Kinetics of Cobalt Sulfides Yolk-Shell Spheres by Anion Doping for Advanced Lithium and Sodium Storage, *ChemSusChem*, 2020, **13**, 4078–4085.

53 Y. Liu, S. Niu and R. Hu, Preparation and supercapacitive performance of manganese-cobalt sulfide/silver nano-wires/graphene ternary nanocomposites, *J. Mater. Sci.: Mater. Electron.*, 2021, **32**(11), 14337–14346.

54 M. S. Javed, H. Lei, J. Li, Z. Wang and W. Mai, Construction of highly dispersed mesoporous bimetallic-sulfide nanoparticles locked in N-doped graphitic carbon nanosheets for high energy density hybrid flexible pseudocapacitors, *J. Mater. Chem. A*, 2019, **7**, 17435.

55 M. R. Pallavolu, S. Vallem, R. R. Nallapureddy, S. Adem and S. W. Joo, Self Assembled Hierarchical Silkworm-Type Bimetallic Sulfide (NiMo3S4) Nanostructures Developed on S-g-C₃N₄ Sheets: Promising Electrode Material for Supercapacitors, *ACS Appl. Energy Mater.*, 2023, **6**, 812–821.

56 Q. Shao, X. Liu, J. Dong, L. Liang, Q. Zhang, P. Li, S. Yang, X. Zang and N. Cao, Vulcanization Conditions of Bimetallic Sulfides Under Different Sulfur Sources for Supercapacitors: A Review, *J. Electron. Mater.*, 2023, **52**, 1769–1784.

57 G. Fang, Z. Wu, J. Zhou, C. Zhu, X. Cao, T. Lin, Y. Chen, C. Wang, A. Pan and S. Liang, Observation of Pseudocapacitive Effect and Fast Ion Diffusion in Bimetallic Sulfides as an Advanced Sodium-Ion Battery Anode, *Adv. Energy Mater.*, 2018, **8**, 1703155.

58 X. Chen, Q. Liu, T. Bai, W. Wang, F. He and M. Ye, Nickel and cobalt sulfide-based nanostructured materials for electrochemical energy storage devices, *Chem. Eng. J.*, 2021, **409**, 127237.

59 D. Li, Y. Gong and C. Pan, Facile synthesis of hybrid CNTs/NiCo$_2$S$_4$ composite for high performance super-capacitors, *Sci. Rep.*, 2016, **6**, 29788.

60 L. Shen, L. Yu, H. B. Wu, X. Y. Yu, X. Zhang and X. W. Lou, Formation of nickel cobalt sulfide ball-in-ball hollow spheres with enhanced electrochemical pseudo-capacitive properties, *Nat. Commun.*, 2015, **6**, 6694.

61 P. Wu, S. Cheng, M. Yao, L. Yang, Y. Zhu, P. Liu, O. Xing, J. Zhou, M. Wang, H. Luo and M. Liu, A Low-Cost, Self-Standing NiCo$_2$S$_4$@CNT/CNT Multilayer Electrode for Flexible Asymmetric Solid-State Supercapacitors, *Adv. Funct. Mater.*, 2017, **27**, 1702160.

62 F. Lu, M. Zhou, W. Li, Q. Weng, C. Li, Y. Xue, X. Jiang, X. Zeng, Y. Bando and D. Golberg, Engineering sulfur vacancies and impurities in NiCo$_2$S$_4$ nanostructures toward optimal supercapacitive performance, *Nano Energy*, 2016, **26**, 313–323.

63 Y. Han, S. Sun, W. Cui and J. Deng, Multidimensional structure of CoNi$_2$S$_4$ materials: structural regulation promoted electrochemical performance in a supercapacitor, *RSC Adv.*, 2020, **10**, 7541.

64 W. Hu, R. Chen, W. Xie, L. Zou, N. Qin and D. Bao, CoNi$_2$S$_4$ Nanosheet Arrays Supported on Nickel Foams with Ultrahigh Capacitance for Aqueous Asymmetric Supercapacitor Applications, *ACS Appl. Mater. Interfaces*, 2014, **6**, 19318–19326.

65 L. Chen, J. Wan, L. Fan, Y. Wei and J. Zou, Construction of CoNi$_2$S$_4$ hollow cube structures for excellent performance asymmetric supercapacitors, *Appl. Surf. Sci.*, 2021, **570**, 151174.

66 X. Zheng, X. He, J. Jiang, Z. Jia, Y. Li, Z. Wei and H. Yang, High-Performance Asymmetric Supercapacitors Based on the Ni$_{1.5}$Co$_{1.5}$S$_4$@CNTs Nanocomposites, *NANO: Brief Rep. Rev.*, 2020, **15**, 2050136.

67 F. Jin, X. He, J. Jiang, W. Zhu, J. Dai and H. Yang, Synthesis of Hierarchical Porous Ni$_{1.5}$Co$_{1.5}$S$_4$/g-C$_3$N$_4$ Composite for Supercapacitor with Excellent Cycle Stability, *Nanomaterials*, 2020, **10**, 1631.

68 L. Yu, L. Zhang, H. B. Wu and X. W. Lou, Formation of Ni$_x$Co$_{3-x}$S$_4$ Hollow Nanoprisms with Enhanced Pseudocapacitive Properties, *Angew. Chem., Int. Ed.*, 2014, **53**, 3711–3714.

69 F. Yang, Z. Fang, K. Xu, J. Yang and J. Hu, Ni$_x$Co$_{3-x}$S$_4$@NiCo$_2$O$_4$ hybrid composites as super-capacitors electrode material, *Mater. Lett.*, 2017, **191**, 101–104.

70 D. Cao, W. Kang, S. Wang, Y. Wang, K. Sun, L. Yang, X. Zhou, D. Sun and Y. Cao, In situ N-doped carbon modi-fied (Co$_{0.5}$Ni$_{0.5}$)$_9$S$_8$ solid-solution hollow spheres as high-capacity anodes for sodium-ion batteries, *J. Mater. Chem. A*, 2019, **7**, 8268.

71 L. Jin, B. Liu, Y. Wu, S. Thanneeru and J. He, Synthesis of Mesoporous CoS$_2$ and Ni$_x$Co$_{1-x}$S$_2$ with Superior Supercapacitive Performance Using a Facile Solid-Phase Sulfurization, *ACS Appl. Mater. Interfaces*, 2017, **9**, 36837–36848.

72 G. Li and C. Xu, Hydrothermal synthesis of 3D Ni$_x$Co$_{1-x}$S$_2$ particles/graphene composite hydrogels for high perform-ance supercapacitors, *Carbon*, 2015, **90**, 44–52.

73 C. Huang, A. Gao, Z. Zhu, F. Yi, M. Wang, J. Hao, H. Cheng, J. Ling and D. Shu, Metal organic frameworks derive d Ni-dope d hierarchical Ni$_x$Co$_{1-x}$S@C bundled-like nanostructures for enhanced supercapacitors, *Electrochim. Acta*, 2022, **406**, 139872.

74 J. Yang, M. Ma, C. Sun, Y. Zhang, W. Huang and X. Dong, Hybrid NiCo$_2$S$_4$@MnO$_2$ heterostructures for high-per-formance supercapacitor electrodes, *Mater. Chem. A*, 2015, **3**, 1258.

75 D. Wang, Y. X. Chang, Y. R. Li, S. L. Zhang and S. L. Xu, Well-dispersed NiCoS$_2$ nanoparticles/rGO composite with a large specific surface area as an oxygen evolution reac-tion electrocatalysts, *Rare Met.*, 2021, **40**(11), 3156–3165.

76 T. Zhu, G. Zhang, T. Hu, Z. He, Y. Lu, G. Wang, H. Guo, J. Luo, C. Lin and Y. Chen, Synthesis of NiCo$_2$S$_4$-based nanostructured electrodes supported on nickel foams with superior electrochemical performance, *J. Mater. Sci.*, 2016, **51**, 1903–1913.

77 M. Dong, Z. Chai1, J. Li and Z. Wang, One-step potentio-static electrodeposition of cross-linked bimetallic sulfide nanosheet thin film for supercapacitors, *Ionics*, 2020, **26**, 4095–4102.

78 N. Jabeen, Q. Xia, M. Yang and H. Xia, Unique Core-Shell Nanorod Arrays with Polyaniline Deposited into Mesoporous NiCo$_2$O$_4$ Support for High-Performance Supercapacitor Electrodes, *ACS Appl. Mater. Interfaces*, 2016, **8**, 6093–6100.

79 S. Ahmed, M. Ahmad, M. H. Yousaf, S. Haider, Z. Imran, S. S. Batool, I. Ahmad, M. I. Shahzad and M. Azeem, Solvent-free synthesis of NiCo$_2$S$_4$ having the metallic nature, *Front. Chem.*, 2022, **10**, 1027024.

80 N. K. Mishra, A. K. Singh, R. Mondal and P. Singh, NiC$_2$O$_4$·2H$_2$O Nanoflakes: A Novel Redox-mediated Intercalative Pseudocapacitive Electrode for Supercapacitor Applications in Aqueous KOH and Neutral Na$_2$SO$_4$ electrolytes, *ChemistrySelect*, 2022, **7**(21), e202201134.

81 B. Zhang, X. Zhang, Y. Wei, L. Xia, C. Pi, H. Song, Y. Zheng, B. Gao, J. Fu and P. K. Chu, General synthesis of

NiCo alloy nanochain arrays with thin oxide coating: a highly efficient bifunctional electrocatalyst for overall water splitting, *J. Alloys Compd.*, 2019, **797**, 1216–1223.

82 A. Gupta, V. Kushwaha, *et al.*, $SrFeO_{3-\delta}$: a novel Fe^{4+}-Fe^{2+} redox mediated pseudocapacitive electrode in aqueous electrolyte, *Phys. Chem. Chem. Phys.*, 2022, **24**, 11066–11078.

83 B. Pattanayak, P. A. Le, D. Panda, F. M. Simanjuntak, K. H. Wei, T. Winie and T. Y. Tseng, Ion accumulation-induced capacitance elevation in a microporous graphene-based supercapacitor, *RSC Adv.*, 2022, **12**, 27082.

84 B. Pal, S. Yang, S. Ramesh, V. Thangadurai and R. Jose, Electrolyte selection for supercapacitive devices: a critical review, *Nanoscale Adv.*, 2019, **1**(10), 3807–3835.

85 L. Zhang, Z. Zeng, D. W. Wang, Y. Zuo, J. Chen and X. Yan, Magnetic field-induced capacitance change in aqueous carbon-based supercapacitors, *Cell Rep. Phys. Sci.*, 2021, **2**, 100455.

86 B. Evanko, S. W. Boettcher, S. J. Yoo and G. D. Stucky, Redox-Enhanced Electrochemical Capacitors: Status, Opportunity, and Best Practices for Performance Evaluation, *ACS Energy Lett.*, 2017, **2**, 2581–2590.

87 S. Fleischmann, J. B. Mitchell, R. Wang, C. Zhan, D. Jiang, V. Presser and V. Augustyn, Pseudocapacitance: From Fundamental Understanding to High Power Energy Storage Materials, *Chem. Rev.*, 2020, **120**, 6738–6782.

88 S. Ardizzone, G. Fregonara and S. Trasatti, "Inner" And "Outer" Active Surface of RuO_2 Electrodes, *Electrochim. Acta*, 1990, **35**, 263–267.

89 J. Wang, J. Polleux, J. Lim and B. Dunn, Pseudocapacitive Contributions to Electrochemical Energy Storage in TiO_2 (Anatase) Nanoparticles, *J. Phys. Chem. C*, 2007, **111**, 14925–14931.

90 R. Kumar and M. Bag, Quantifying Capacitive and Diffusion-Controlled Charge Storage from 3D Bulk to 2D Layered Halide Perovskite-Based Porous Electrodes for Efficient Supercapacitor Applications, *J. Phys. Chem. C*, 2021, **125**, 16946–16954.

91 N. K. Mishra, R. Mondal, T. Maiyalagan and P. Singh, Synthesis, Characterizations, and Electrochemical Performances of Highly Porous, Anhydrous $Co_{0.5}Ni_{0.5}C_2O_4$ for Pseudocapacitive Energy Storage Applications, *ACS Omega*, 2022, **7**, 1975–1987.

92 A. N. Singh, K. G. Nigam, R. Mondal, V. Kushwaha, A. Gupta, C. Rath and P. Singh, Effect of strontium doping on the electrochemical pseudocapacitance of $Y_{1-x}Sr_xMnO_{3-\delta}$ perovskites, *Phys. Chem. Chem. Phys.*, 2023, **25**, 326.

93 D. Mohanadas and M. A. A. M. Abdah, Facile synthesis of PEDOT-rGO/HKUST-1 for high performance symmetrical supercapacitor device, *Sci. Rep.*, 2021, **11**, 11747.

94 P. Wu, S. Cheng, M. Yao, L. Yang, Y. Zhu, P. Liu, O. Xing, J. Zhou, M. Wang, H. Luo and M. Liu, A Low-Cost, Self-Standing $NiCo_2O_4$@CNT/CNT Multilayer, *Adv. Funct. Mater.*, 2017, **27**, 1702160.

95 C. Xia, P. Li, A. N. Gandi, U. Schwingenschlögl and H. N. Alshareef, Is $NiCo_2S_4$ Really a Semiconductor, *Chem. Mater.*, 2015, **27**, 6482–6485.

96 Y. Gao, L. Mi, W. Wei, S. Cui, Z. Zheng, H. Hou and W. Chen, Double Metal Ions Synergistic Effect in Hierarchical Multiple Sulfide Microflowers for Enhanced Supercapacitor Performance, *ACS Appl. Mater. Interfaces*, 2015, **7**, 4311–4319.

97 W. Chen, C. Xia and H. N. Alshareef, One-Step Electrodeposited Nickel Cobalt Sulfide Nanosheet Arrays for High-Performance Asymmetric Supercapacitors, *ACS Nano*, 2014, **8**(9), 9531–9541.

98 S. S. Singha, S. Rudra, S. Mondal, M. Pradhan, A. K. Nayak, B. Satpati, P. Pal, K. Das and A. Sinha, Mn incorporated MoS_2 nanoflowers: A high-performance electrode material for symmetric supercapacitor, *Electrochim. Acta*, 2020, **338**, 135815.

99 S. X. Yan, S. H. Luo, J. Feng, L. Yang, P.-W. Li, Q. Wang, Y. H. Zhang, X. Liu and L. J. Chang, Asymmetric, Flexible Supercapacitor Based on Fe–Co Alloy@Sulfide with High Energy and Power Density, *ACS Appl. Mater. Interfaces*, 2021, **13**, 49952–49963.

100 F. Lu, M. Zhou, W. Li, Q. Weng, C. Li, Y. Xue, X. Jiang, X. Zeng, Y. Bando and D. Golberg, Engineering sulfur vacancies and impurities in $NiCo_2S_4$ nanostructures toward optimal supercapacitive performance, *Nano Energy*, 2016, **26**, 313–323.

101 Q. Xia, L. Si, K. Liu, A. Zhou, C. Su, N. M. Shinde, G. Fan and J. Dou, In Situ Preparation of Three-Dimensional Porous Nickel Sulfide as a Battery-Type Supercapacitor, *Molecules*, 2023, **28**, 4307.

102 M. Singh, S. Kumar, R. Mondal, P. Singh, R. Prakash and N. Sharma, Combustion-Synthesized $KNiPO_4$: A Non-toxic, Robust, Intercalating Battery-Type Pseudocapacitive Electrode for Hybrid Supercapacitors as a Large-Scale Energy Storage Solution, *Energy Fuels*, 2023, **37**, 4094–4105.

103 Q. Li, F. Yu, Y. Cui, J. Wang, Y. Zhao and J. Peng, Multilayer SnS-SnS_2@GO heterostructures nanosheet as anode material for Sodium ion battery with high capacity and stability, *J. Alloys Compd.*, 2023, **937**, 168392.